An overview on the use of backscattered sound for measuring suspended particle size and concentration profiles in non-cohesive inorganic sediment transport studies.

Peter D. Thorne[1] and David Hurther[2]

1. National Oceanography Centre, Joseph Proudman Building, 6 Brownlow Street, Liverpool, L3 5DA, United Kingdom.

2. Laboratory of Geophysical and Industrial Flows (LEGI), CNRS UMR 5519, Grenoble University, France

*Corresponding author. Email: pdt@noc.ac.uk, Tel: +44 151 795 4862

16/10/13

23

24

25

26   **ABSTRACT**

27

28   For over two decades, coastal marine scientists studying boundary layer sediment transport

29   processes have been using, and developing, the application of sound for high temporal-spatial

30   resolution measurements of suspended particle size and concentration profiles. To extract the

31   suspended sediment parameters from the acoustic data requires an understanding of the

32   interaction of sound with a suspension of sediments and an inversion methodology. This

33   understanding is distributed around journals in a number of scientific fields and there is no single

34   article that succinctly draws together the different components. In the present work the aim is to

35   provide an overview on the acoustic approach to measuring suspended sediment parameters and

36   assess its application in the study of non-cohesive inorganic suspended sediment transport

37   processes.

38

39

40   Keywords: Overview analysis. Sandy suspended sediments. Size and concentration profiles.
41   Multi-frequency acoustic backscattering. Inversion methodologies. Sediment transport processes

42

43   **List of main parameters and their units**

44

45   a. Particle radius (m)

46   a_o. Mean radius based on $n(a)$. (m)

47   a_c. Mean radius of the suspension field based on $n(a)$. (m)

48   a_m. Mean radius based on $m(a)$. (m)

49   a_M Acoustic estimate of the suspended particle radius. (m)

50   a_r. Reference value for a_c at z_r. (m)

51   a_{50}. Median mass radius based on $m(a)$ (m)

52   A_t. Transducer radius. (m)

53   C. Suspended concentration field. (kgm^{-3})

54   C_r. Reference value for C at z_r. (kgm^{-3})

55   d_{50}. Median mass diameter based on $m(a)$ (m)

56   f_i. Intrinsic backscatter form function. (-)

57   f. Ensemble density normalised backscatter form function. (kg$^{-1/2}$m$^{3/2}$)

58   j. Frequency counter used in the inversion.

59   k. Acoustic wavenumber, $2\pi/\lambda$. (m^{-1})

60   K. Sediment backscattering property. (kg$^{-1/2}$m)

61    $m(a)$. Particle mass radius probability density function. (-)

62   M_o. Initial acoustic estimate of the suspended concentration. (kgm^{-3})

63   M. Acoustic estimate of the suspended concentration. (kgm^{-3})

64    $n(a)$. Particle number radius probability density function. (-)

65   N. Number of frequencies used in the inversion.

66   r. Range from the transducer. (m)

67   r_n. Transducer nearfield, $\pi A_t^2/\lambda$. (m)

68    $\Re$. The system constant. (Vm$^{3/2}$)

69   V. Backscattered signal. (V)

70   V_m^2. Mean-square backscattered signal. (V^2)

71    $x=ka$. (-), $x_o=ka_o$. (-)

72   z. Height above the bed. (m)

73   z_r. Reference height, $z_r=0.005$. (m).

74   α_w. Attenuation due to water absorption. (Nepers m^{-1})

75   α_s. Attenuation due to sediment scattering. (Nepers m^{-1})

76   γ_o. Random error introduced into the backscattered signal (-)

77   δ. Normalised standard deviation. (-)

78   ε. Systematic error introduced into the backscattered signal (-)

79   η. Number of independent samples. (-)

80   λ. Wavelength of sound. (m)

81   ξ. Sediment attenuation constant. (kg^{-1}m^2)

82   ρ. Sediment grain density. (kgm^{-3})

83   σ. Standard deviation. (units depend on parameter)

84   σ_e. Standard error. (units depend on parameter)

85   τ. Time lag. (s)

86   τ_o. Decorrelation time lag. (s)

87   Φ. Parameter used to estimate acoustical particle radius (-)

88   χ_i. Intrinsic normalised total scattering cross-section. (-)

89   χ. Ensemble density normalised mean normalised total scattering cross-section. (kg^{-1}m^3)

90   ψ. Transducer nearfield correction. (-)

91

92

93   1. Parameters in the text with subscript 'b' refers to bed sediments.

94   2. $\overline{X}$. Overbar represents a time averaged parameter.

95   3. $\overline{X/Y}$. Overbar represents a time and height averaged parameter.

96

1. INTRODUCTION

It is readily acknowledged that one of the most important processes in the coastal environment is the movement of sediments; they impact on habitats, water quality, turbidity, biogeochemistry and morphology (Davies and Thorne, 2008; Amoudry and Souza, 2011). Therefore improving our capability to monitor and model sediment transport in the marine environment is an essential component of sustainable development and management. In particular as detailed physics based process models have developed, there has been the requirement to measure sediment dynamics with increasing temporal-spatial resolution (van der Werf et al, 2008). This has led to the development of new technologies and the utilisation of acoustics has been one of the competitors in this field (Thorne and Hay, 2012).

On the larger scale acoustic Doppler current profilers, ADCP, have been around for three decades measuring flow profiles (Gordon 1996) and more recently the amplitude of the backscattered signal has been used to estimate suspended concentration (Holdaway et al, 1999; Moore et al, 2012; Moore et al, 2013). Further in the last year or two there has also been the application of using swath bathymetry systems to measure suspended sediments (Simmons et al 2010). On the smaller scale significant advances have been taking place in the application of sound to the study of near-bed sediment transport processes (Vincent et al, 1999; Hurther and Thorne, 2011; Bolanos et al, 2012; Hay et al 2012). Acoustics has and is being developed for near-bed studies because it is recognised as having the potential to measure non-intrusively, co-located, simultaneously and with high spatial-temporal resolution, suspended sediment and flow profiles and provide information on bedforms. This has lead to the development of multi-frequency acoustic backscatter systems, ABS, to measure suspended particle size and concentration (Crawford and Hay, 1993; Thorne and Hardcastle, 1997), high resolution acoustic Doppler velocity profilers, ADVP, for turbulent and intra-wave observations (Hurther et al 2007; Hay et al 2012), combined systems for high resolution acoustic concentration and velocity profiles, ACVP, (Hurther et al 2011) and two and three dimensional acoustic ripple profiles, ARP, to provide detailed bedform measurements with sub-centimetric resolution (Traykovski, 2007; Hay, 2011; O'Hara Murray et al, 2012). Developments using acoustic near-bed systems have been presented in the literature (Thorne and Hanes, 2002; Hurther et al 2011).

128

The present work focuses on the near-bed application and forms the third part of a trilogy on ABS systems in which the first part described the system calibration using suspensions with known scattering characteristics (Betteridge et al, 2008), the second centred on acoustic scattering properties of suspended marine sediments (Thorne and Meral, 2008; Moate and Thorne, 2012) and here the study focuses upon the extraction of suspended sediment parameters from the backscattered acoustic data. The literature associated with the application of acoustics to the measurement of suspended sediment measurements is distributed amongst journals in the fields of acoustics (Sheng and Hay, 1998; Thosteson and Hanes, 1998; Moate and Thorne, 2009), engineering (Thorne et al, 1994; Hurther et al, 2011), sedimentology (Vincent et al, 1991; O'Hara Murray et al, 2012; Pedocchi and Garcia 2012) and geosciences (Hay and Sheng, 1992; Vincent et al, 1999; Hurther and Thorne 2011) with no single article providing an overview of the approach. It was therefore considered timely, given the expanding use of sound for measuring suspended sediments, that an article providing such an overview of the topic would be of value to coastal marine scientists who are using, or beginning to use acoustics, in bottom boundary layer sediment transport studies.

144

Examined here is the inversion of acoustic data backscattered from inorganic non-cohesive suspended sediments and its application to the measurement of suspended particle size and concentration profiles. The intention is to provide a description of the commonly adopted inversion approach used with contemporary ABS deployed in sandy marine environments. To this end a series of formulations are described which cover a range of inversions from simple to more complex approaches. Depending on the availability of independent information on the suspension, the inversion may be more or less subject to uncertainty. Here an assessment is made of the inversion process and how different factors impact on the calculated acoustic estimates of suspended particle size and concentration. The relationship between the measured acoustic parameters and those commonly used in sediment transport models is discussed. The influence of the system calibration accuracy, the uncertainty in the scattering properties of the sediments, the effect of the particle size distribution, the frequencies to use and the impact of signal averaging are all considered in the assessment. The specific impact of extraneous scatterers such as bubbles, organic particles and living organisms on the acoustic inversion is not explicitly

159   investigated in this study, although the extraneous scatterers could be considered as contributing

160   to the systematic and random errors introduced into the backscattered signals used in the study.

161

162   To carry out the inversion assessment, a suspension field is simulated, sound propagated through

163   the field and the backscattered signal calculated. It is this backscattered signal which is inverted

164   using a number of formulations, from simple to more complex in a number of scenarios. The

165   suspension field used is based on observations collected in coastal environments. The time-

166   averaged vertical profile of suspended sediment concentration corresponds to a standard Rouse

167   profile. In the absence of a general theory for vertical grain size sorting a time-averaged vertical

168   profile based on a power law is employed. This formulation comes from observations collected

169   in a wave dominated rippled environment (Thorne et al., 2011a). Although this size profile is not

170   necessarily appropriate to highly turbulent suspension flows when size sorting may be ignored, it

171   does offers a flow regime for testing the full performance of the acoustic profiling of both

172   sediment concentration and grain size. Superimposed upon the mean profiles are temporal

173   fluctuations to represent turbulence and wave motion and assessment is made as to how well

174   these fluctuation are represented in the acoustic inversions.

175

176   The   software   underpinning   the   results   presented   in   the   paper   can   be   found   at

177   **************************************. The software consists of MATLAB programs

178   which calculate the suspension field, the sediment scattering characteristics, the backscattered

179   voltage with systematic and random errors and inversions to calculate the acoustically estimated

180   concentration field, and the particle size and concentration fields. The software is an

181   investigative tool for academic/student use and is not supported by the authors or their institutes.

182

183

184 **2. SCATTERING FORMULATION AND INVERSION**

185 The theory of scattering from an aqueous suspension of particles has been previously presented

186 (Sheng and Hay, 1988; Hay, 1991; Crawford and Hay, 1993; Thorne et al, 1993; Thorne and

187 Hardcastle, 1997) and is summarised in Appendix 1 to provide the background to equation (1)

188 below. For the normally deployed disc transceivers used for both transmission and reception,

189 insonifying a suspension of sediments, then for the usual conditions of incoherent scattering

190 (Morse and Ingard, 1987), the acoustically measured suspended concentration, M, can be related

191 to the mean-squared backscattered voltage, V_m^2, as shown below (Hay and Sheng, 1992; Thorne

192 and Hanes, 2002; Hurther et al, 2011)

193
$$M = \left(\frac{r\psi}{K\,\Re}\right)^2 V_m^2 \, e^{4(r\alpha_w + \alpha_s)} \tag{1}$$

194 where

$$K = \frac{f}{\sqrt{a_0}} \, , \qquad \alpha_s = \int_0^r \xi M \, dr \, , \qquad \xi = \frac{3\chi}{4a_o}$$

$$\psi = \frac{1 + 1.35\left(\frac{r}{r_n}\right) + (2.5\frac{r}{r_n})^{3.2}}{1.35\left(\frac{r}{r_n}\right) + (2.5\frac{r}{r_n})^{3.2}}$$

195 with

$$f(x_o) = \left[\frac{\int_0^\infty an(a)da \int_0^\infty a^2 \left(\frac{f_i}{\sqrt{\rho}}\right)^2 n(a)da}{\int_0^\infty a^3 n(a)da}\right]^{1/2} \tag{2a}$$

196

$$\chi(x_o) = \frac{\int_0^\infty an(a)da \int_0^\infty a^2 \left(\frac{\chi_i(x)}{\rho}\right) n(a)da}{\int_0^\infty a^3 n(a)da} \tag{2b}$$

197

198
$$a_o = \int_0^\infty an(a)da \tag{2c}$$

199 and

$$\frac{f_i}{\sqrt{\rho}} = \frac{\left(1 - 0.25e^{-((x-1.5)/0.35)^2}\right)\left(1 + 0.6e^{-((x-2.9)/1.15)^2}\right)x^2}{42 + 25x^2} \tag{3a}$$

$$\frac{\chi_i}{\rho} = \frac{0.09x^4}{1380 + 560x^2 + 150x^4} \tag{3b}$$

200   r is the range from the transceiver and ψ accounts for the departure from spherical spreading

201   within the transducer nearfield (Downing et al 1995), $r_n = \pi A_t^2/\lambda$ is the transducer nearfield, A_t is

202   the transducer radius, $\Re$ is the system constant incorporating the transmit and receive sensitivity,

203   the voltage transfer function for the system, the pulse length and the directivity function of the

204   transceiver (Betteridge et al 2008). K represents the sediment backscattering properties, ρ is the

205   sediment grain density and a_o is the suspension mean particle radius. The term α_ω is the sound

206   attenuation due to water absorption and α_s is the attenuation due to suspended sediment

207   scattering. f_i and χ_i are respectively the intrinsic form function and intrinsic normalised total

208   scattering cross-section for the particles in suspension and x=ka, where k is the wavenumber of

209   the sound and a is the radii of the particles in suspension. Here intrinsic refers to the scattering

210   characteristics measured using suspensions sieved into narrow ¼ phi size fractions which

211   provide a nominally single particle size (Hay, 1991). Physically, f_i describes the backscattering

212   characteristics of a particle relative to its geometrical size, whilst χ_i quantifies the scattering from

213   a particle over all angles, relative to its cross sectional area, and is proportional to scattering

214   attenuation. There are a number of similar expressions for f_i and χ_i (Sheng and Hay 1988;

215   Crawford and Hay, 1993; Thorne and Meral, 2008) and here we have chosen to present a

216   recently developed density normalised expressions which has generic applicability to sands of

217   varying mineralogy (Moate and Thorne, 2012). f and χ represent the ensemble mean scattering

218   values obtained by integrating the intrinsic scattering characteristics over the particle size

219   probability density function, n(a), of the particles in suspension and $x_o = ka_o$. So as not to over

220   complicate the inversions presented, particle viscous absorption (Richards et al 2003) for x<<1,

221   and the sinh(*B*)/*B* function (Hay, 1991; Thosteson and Hanes 1998) required at concentrations in

222   the tens of kgm^{-3}, are neglected. These are not particularly restrictive limitations in sandy coastal

223   environments using low megahertz frequency ABS.

224

225   Although equation (1)-(3) may appear somewhat complex, there are degrees of simplification

226   that can be made depending on the required accuracy and detail on the suspension. These are

227   explored for a number of cases below.

228

229

230   *2.1. Estimating the suspended sediment concentration*

231

232   Equation (1) is implicit with M being on either side of the equation due to the effect of

233   attenuation by the presence of the sediments themselves. If the sediment attenuation can be

234   assumed negligible, $r\alpha_s \ll 1$, the equation becomes explicit and its evaluation is simplified. Further

235   if only the far field is considered, $\psi=1$, equation (1) can be written as

236

237    $$M_o = \left(\frac{r}{K\Re}\right)^2 V_m^2 \, e^{4r\alpha_w}$$ (4)

238

239   For this case, after allowing for α_w (Clay and Medwin, 1997), the concentration at any range is

240   simply proportional to the mean-square backscattered signal. To evaluate equation (4) requires a

241   value for $K\Re$. Normally bed samples are collected when instruments are deployed and laboratory

242   calibrations can be carried out using a suspension of the bed material. By using backscatter data

243   collected in the far-field, at sufficiently low concentrations such that $r\alpha_s \ll 1$, the calibration is

244   given by

245

246    $$(K\Re)^2 = \frac{r^2 V_m^2}{C} e^{4r\alpha_w}$$ (5)

247

248   Since C is the measured concentration used in the calibration and α_w can be calculated, $K\Re$ can

249   be readily obtained. However, this calibration includes the sediment backscattering

250   characteristics, K, which is site specific, based on the bed sediments and invariant with height

251   above the bed and time. It also presupposes that the suspended sediments in the field have a size

252   distribution equal to the bed. The approach only requires a single frequency ABS and provides a

253 simple, though limited, calibration for estimating concentration profiles collected at a particular

254 field site.

255

256 As mentioned above equation (5) provides a site specific calibration. However, if use is made of

257 equation (3a) to obtain $f_i/\sqrt{\rho}$ and combined with a measurement of n(a) of the bed, this allows

258 $f(x_o)$ and a_o to be evaluated using equations (2a) and (2c) and K calculated. The value for $\Re$ can

259 then be estimated; this is an instrument parameter and is independent of the deployment site.

260 With $\Re$ known the single frequency ABS system can be deployed at any site and with a

261 measurement or estimate for n(a), $f(x_o)$ and a_o can be calculated, K obtained for the deployment

262 site, and inversions carried out to obtain concentration profiles, subject to the assumption of size

263 invariance with height and time. Using a suspension of sediments to provide $\Re$ leads to a

264 nominal value because the formulation for $f_i/\sqrt{\rho}$ in equation (3a) is a generic mean expression

265 derived from a number of data sets (Moate and Thorne, 2012). To obtain a precise value for $\Re$

266 requires the scattering properties, and hence K, for the suspension to be precisely known, this can

267 be obtained using suspensions of spheres which have an exact analytical scattering solution

268 (Faran, 1951; Gaunaurd and Uberall, 1983; Betteridge et al, 2008).

269

270 When α_s cannot be assumed to be negligible equation (1) becomes implicit, with M on either side

271 of the equation and the inversion becomes slightly more complicated. If the system has been

272 calibrated as discussed above and K$\Re$, or $\Re$ is known and n(a) measured or estimated, equation

273 (4) can be evaluated and M_o profiles calculated, preferably with the nearfield correction term, ψ,

274 included. An improved estimate for M can be obtained using the expressions in equation (1) to

275 estimate α_s, by calculating ξ with the formulation for χ_i/ρ given by equation (3b) with n(a) to

276 obtain χ using equation (2b) and evaluating

$$M_1 = M_o e^{4\alpha_{so}} \tag{6}$$

278 The value for α_{so} is calculated using M_o. In general equation (6) can be written as

$$M_{\kappa+1} = M_o e^{4\alpha_{s\kappa}} \tag{7}$$

280 Equation (7) is iterated until a convergence criterion has been satisfied and the value for M at the
281 first range bin evaluated. The iterative process is repeated sequentially stepwise at each range bin
282 through the V_m^2 profile, with the accumulating sediment attenuation accounted for and the profile
283 of M with r from the transducer progressively calculated (Hay and Sheng, 1992; Thorne and
284 Hardcastle; 1997; Thorne et al, 2011b).

285

286 *2.2. Estimating the mean particle size and suspended sediment concentration*

287

288 Apart from the site specific calibration, it has been assumed that in the evaluation of equation (4)
289 the suspended particle size distribution is known or estimated and that it is invariant over the
290 deployment period of the ABS. If the size is unknown or its temporal variability with height
291 above the bed is required, this necessitates the ABS system to operate at more than one
292 frequency. This is not a particular constraint as most ABS systems deployed are multi-frequency
293 (Hay and Sheng; 1992; Thorne and Hardcastle 1997; Villard et al 2000; O'Hara Murray, 2012).
294 It does, however, require $\Re$ to be obtained at each frequency as described above. Using the
295 differential scattering characteristic of the suspended sediments with frequency, profiles of the
296 acoustic measurement of particle radius, a_M, an estimate for a_o, can be made with M. This still
297 requires an estimate for n(a), although a_M is calculated from the inversion. A number of
298 approaches have been used to obtain a_M (Hay and Sheng, 1992; Crawford and Hay, 1993;
299 Thosteson and Hanes, 1998; Moore et al, 2013) and the approach adopted here which has been
300 found to be relatively robust is that of Thorne et al (2007) and Moate and Thorne (2012).

301

302 Using the approach of Thorne et al (2007), for the case when $r\alpha_s \ll 1$, f is calculated using
303 equations (2a) and (3a) with n(a) and K_j evaluated at each of the N frequencies in the ABS
304 system, where subscript j=1:N, over a range of a_o which covers the expected mean particle radius
305 variation in suspension. Using these values of $K_j(a_o)$ with V_{mj}^2, $M_{oj}(a_o)$ is calculated using
306 equation (4) and the parameter Φ evaluated for each value of a_o over the range of a_o as below

307
$$\Phi = \frac{\sigma_M(a_o)}{M_o(a_o)} \tag{8}$$

$$M_o(a_o) = \frac{1}{N}\sum_{j=1}^{N} M_{oj}(a_o) \qquad \sigma_M^2(a_o) = \frac{1}{N}\sum_{j=1}^{N} M_{oj}^2(a_o) - [M_o(a_o)]^2$$

308   The value of a_o for which Φ is a minimum at each range gate provides profiles of a_M and M_o over

309   the deployment period. Illustrations of this process and the form of Φ are presented in Appendix

310   2. When α_s is not negligible the additional complication of an implicit iterative inversion is

311   required. The procedure uses equations (4), (6) and (7), with χ calculated using equations (2b)

312   and (3b) with n(a), for the range of a_o, at each frequency, and equation (8) evaluated with M

313   replacing M_o. The implicit iterative process is repeated sequentially stepwise at each range bin

314   through the V_{mj}^2 profiles, with the accumulating sediment attenuation accounted for and the

315   profiles of a_M and M with r from the transducer progressively calculated (Thorne et al 2011b).

316   This is the full inversion of equation (1) when the temporal-spatial structure of a_M and M for the

317   suspension field is required.

318

319   *2.3 Scattering properties and sediment size distribution*

320   In equation (3) the density normalized intrinsic scattering properties, $f_i/\sqrt{\rho}$ and χ_i/ρ are given,

321   however, invariably, in the marine environment, there will be a particle size distribution and the

322   ensemble scattering characteristics described in equation (2), f and χ, are required. It is therefore

323   important to assess how n(a) impacts on the suspension scattering characteristics. To assess this

324   three common probability density functions for the size were examined; the normal, $n_n(a)$,

325   lognormal, $n_l(a)$, and bi-normal, $n_{bi}(a)$. These are respectively given by;

326

327    $$n_n(a) = \frac{1}{\sigma\sqrt{2\pi}} e^{-(a-a_o)^2/2\sigma^2} \qquad\qquad (9a)$$

328

329    $$n_l(a) = \frac{1}{a\zeta\sqrt{2\pi}} e^{-(\log(a)-\gamma)^2/2\zeta^2}, \quad \zeta = \sqrt{\log_e[(\sigma/a_o)^2+1]}, \quad \gamma = \log_e(a_o^2/\sqrt{a_o^2+\sigma^2}) \qquad (9b)$$

330

331    $$n_{bi}(a) = \frac{1}{\sigma_1\sqrt{2\pi}} e^{-(a-a_1)^2/2\sigma_1^2} \frac{1}{\sigma_2\sqrt{2\pi}} e^{-(a-a_2)^2/2\sigma_2^2} \qquad\qquad (9c)$$

13

332

333 For all the distributions the parameters were chosen so that the normalised standard deviation,

334 $\delta=\sigma/a_o$, of n(a) was equal to $\delta=0.4$. A comparison of the distributions are shown in figure 1a for a

335 value of $a_o=100$ μm. The ensemble scattering characteristics f and χ were calculated using

336 equation (2), by integrating the density normalized intrinsic values, $f_i/\sqrt{\rho}$ and χ_i/ρ given in

337 equation (3), over n(a) described in equations (9a)-(9c), and the scattering and attenuation

338 parameters K and ξ evaluated. The results are shown in figures 1b and 1c for a frequency of 2.0

339 MHz; increasing or decreasing the frequency respectively raises or lowers the values of K and ξ,

340 however, the form with x_o remains constant. The solid line represents the intrinsic scattering

341 characteristics and the symbols the ensemble scattering characteristics. As can be seen the impact

342 of the size distribution on the scattering characteristics is to substantially increase values in the

343 Rayleigh regime, $x_o<<1$, while marginally reducing values in the geometric regime, $x_o>>1$

344 (Thorne and Meral, 2008). The departure from the intrinsic scattering properties is similar for the

345 three distributions and scales with the standard deviation. Therefore to first order it is the value

346 for σ which controls the departure from the intrinsic scattering properties, rather than the precise

347 form of n(a). This divergence of the ensemble scattering characteristic from the intrinsic will

348 impact on acoustic inversions and therefore needs to be accounted for when calculating particle

349 size and concentration from acoustic backscattered data.

350 *2.4. Statistics of the backscattered signal*

351 Equation (1) provides an expression for M based on incoherent scattering due to the

352 backscattered signal having random phase statistics uniformly distributed over 2π. To obtain V_m^2,

353 V^2 is average over a number of independent backscattered signals and the number averaged

354 determines the standard error for V_m^2. For incoherent scattering the probability distribution for the

355 backscatter signal, V, is Rayleigh (Hay, 1983; Thorne et al 1993) and for V^2 exponential

356 (Wilhelmij and Denbigh, 1984; Libicki et al, 1989)

357
$$p(V^2) = \beta e^{-(\beta V^2)}$$
(10)

358 where $\beta=1/V_m^2$. For an exponential distribution the standard deviation, $\sigma=1/\beta$, therefore the

359 standard error in V_m^2 is given by

$$360 \qquad\qquad\qquad \sigma_e(V_m^2) = \frac{V_m^2}{\sqrt{\eta}} \qquad\qquad\qquad (11)$$

361   where η is the number of independent profiles averaged to form V_m^2 . Since M is proportional to

362   V_m^2 the normalized standard error in the estimated concentration due to the statistical nature of

363   the backscattered signal is $\sigma_e(M)/M \approx 1/\sqrt{\eta}$. To assess these statistical characteristics, figures 2a

364   and 2b show results from backscatter data collected on a homogeneous suspension of ¼φ sieved

365   magnetite sand of diameter 275 μm, at frequencies of 1.0 (•), 2.93(o), 4.02(Δ) and 4.9(+) MHz,

366   with a pulse length of 10 μs and pulse repetition frequency, prf, of 4 Hz; moderately sorted

367   suspended quartz sand, d_{50}=240 μm σ(d)=83 μm, under waves with a prf of 160 Hz, pulse length

368   of 4 μs and frequency of 1.25 MHz, and from flowing water containing nominally homogeneous

369   micro-bubbles in a open channel with a prf of 95 Hz, a pulse length of 2 μs and a frequency of

370   2.0 MHz. Each data set was normalised by its mean square value so that the results could be

371   compared with a single theoretical prediction, give by the solid line in the figures. As can be

372   seen, for the varied frequencies, pulse repetition frequencies, pulse lengths and scatterer type, the

373   data follow the theoretical predictions, thereby confirming the assumption of incoherent

374   scattering upon which the ABS theoretical analysis is formulated.

375

376   The value for η used to assess the accuracy of M is based on independent samples and therefore

377   it is important to ascertain the decorrelation time to obtain independent samples. To examine the

378   decorrelation, the signal amplitude from an acoustic Doppler velocity profiler (Hurther et al

379   2011) backscattered from suspended sediments under waves and flowing water containing

380   micro-bubbles, were collected using at a pulse repletion frequency respectively of 1600 Hz and

381   952.4 Hz. The measured autocorrelation functions of the backscatter signals with time lag are

382   shown in Figure 2c. The figure clearly shows an initial reduction in the level of the

383   autocorrelation functions followed by a nominally constant value close to zero. The solid line in

384   the plot is a simple empirical fit to the data obtained using $e^{(-\tau/\tau_o)^2}$ where τ is the lag and τ_o=2.0

385   ms. The present results indicate a decorrelation time of around 3-5 ms. Hay and Bowden (1994)

386   using a 2.0 MHz ABS under waves in the field estimated a decorrelation time of 2-4 ms.

387   Therefore if an upper limit of 5 ms is assumed for the decorrelation time, the corresponding

388   maximum pulse repetition for independent samples would be 200 Hz. If 5.0 Hz concentration

389   profiles were required an accuracy of $\sigma(M)/M \approx 0.16$ would result from backscattered profiles

390   collected at 200Hz. If higher accuracy was needed then vertical averaging over independent

391   range bins could be carried out. The importance of the statistical nature of the backscatter signal,

392   and the requirement for averaging over independent samples, is that it may lead to a degree of

393   compromise between the desired spatial-temporal resolution and the degree of averaging

394   necessary to obtain an acceptable accuracy for M.

395

396

3. BACKSCATTERING FROM A SUSPENSION FIELD

3.1 Formulation of the suspended field

To assess the different inversions described in Section 2 requires simulations to be carried out. Therefore to examine the inversion of the backscattered signal and the resulting acoustic estimates of suspended sediment parameters a simulated suspension field through which the sound could be propagated was required. To establish the suspension field the underlying profiles for the time averaged concentration, $\bar{C}$, and the time averaged mean particle radius, $\bar{a}_c$ were of the form

$$\bar{C} = \bar{C}_r \left(\frac{z}{z_r}\right)^{-p} \tag{12a}$$

$$\bar{a}_c = \bar{a}_r \left(\frac{z}{z_r}\right)^{-l} \tag{12b}$$

Equation (12a) is the commonly used Rouse profile (Soulsby, 1997) which approximates to a power law near the bed, p is the Rouse parameter $p=w_s/\kappa u_*$, where u_* is the bed friction velocity, κ is the Von Karman constant and w_s is the particle settling velocity. $\bar{C}_r$ is the reference concentration and for the present study it was specified at the lowest ABS range bin above the bed which was at a height of $z_r=0.005$ m. In the absence of a general theory for the vertical grain size sorting effects and the lack of size sorting measurements in the literature, it is adopted here that $\bar{a}_c$ follows the power law given by equation (12b). This is based on the observations (Thorne et al, 2011a) collected over a rippled sand bed for a range of wave forcing and bed sediment size conditions. For this type of flow, grain size sorting effects are found to be significant resulting in decreasing $\bar{a}_c$ corresponding with the region of the Rouse profile. It is acknowledged that such a form is not generic, for example under highly turbulent conditions for fine sediments $\bar{a}_c$ profiles may be more uniform. Further, vertical temporal differential settling velocities within the suspended size distribution are not specifically addressed in the simulated suspension field. However, the selected ripple suspension conditions are appropriate for testing the full performance of the acoustic profiling of both sediment concentration and grain size when size sorting effects are important. For the present study the variables in equation (12) were given the following values; p=1, l=0.2, $\bar{C}_r$=5.0 kgm^{-3} and $\bar{a}_r$=78 μm.

17

424

As well as requiring a time averaged mean size profile, a size distribution was also required to represent the suspension. Most sedimentologists use a mass probability density function, $m(a)$, to represent particle size and one of the more common distributions fitted to natural sediments is the lognormal given in equation (9b) (Soulsby, 1997). For the acoustic analysis the probability density function required is not $m(a)$, but $n(a)$, which is obtained from $m(a)/a^3$ assuming nominally spherically shaped particles. In Figure 3 is shown the lognormal bed sediment mass probability density function, $m_b(a)$, used in the present study, from which the suspended sediment profiles were derived. The distribution had $\delta_b=0.4$, where $\delta_b=\sigma_{bm}/a_{bm}$, and σ_{bm} and a_{bm} are respectively the standard deviation and mean of $m_b(a)$. For the suspended sediments δ was also set to a value 0.4 and therefore as a_c reduced with height above the bed σ_c proportionally decreased. For the bed $a_{bm}=173\mu m$ and the median grain diameter $2a_{b50}=d_{b50}=320$ μm. Based on the Wentworth scale (Soulsby 1997) this is medium sand. The form for $n_b(a)$ is also shown in figure 3, it is down shifted in radius with its mean value, a_{bc}, being $a_{bc}=0.64a_{bm}$ (110μm), although $n_b(a)$ remains lognormal distributed and retains the same ratio of the standard deviation, σ_{bc}, to mean, $\sigma_{bc}=0.4a_{bc}$. The radius which is measured acoustically, a_M, is an estimate for a_c and this has implications for sediment transport studies. Marine scientists generally use d_{50}, based on $m(a)$, to designate the size of the particles in suspension and it is d_{50} upon which most sediment transport formulations are based (Soulsby 1997). In the present case $\sigma_{bc}=0.4a_{bc}$, $a_{bc}=0.64a_{bm}$, and $d_{b50}=2.9a_{bc}$. Therefore the mean particle diameter, $2a_M$, obtained from an acoustic inversion, which is an estimate for $2a_c$, is not the size used in most sediment formulae; this point is returned to in Section 5.4.

Equation (12) provides the basic formulation for the time averaged suspension field, however to represent the temporal and spatial variability, arising from turbulent and intra-wave fluctuations in the hydrodynamics, periodic and random components were superimposed upon the basic structure. The results for the a_c and C fields are shown in figures 4a and 4d. The temporal and vertical variability portrayed in these figures is considered to be consistent with observations made in the coastal zone (Hay and Bowden, 1994; O'Hare Murray, 2012). The degree of coherence between a_c and C is associated with more dynamic events generating higher concentrations with larger particles sizes, while weaker events have lower concentrations and

455   smaller suspended particles Figures 4b and 4e show the mean profile averaged over the record

456   length, $\bar{a}_c$ and $\bar{C}$, and figures 4c and 4f shows the time series reference values at z=0.005 m. The

457   reference values varied between C_r= 0.7-16 kgm^{-3} and a_r=57-110 µm. It is the suspension fields

458   shown in figures 4a and 4b, combined with the lognormal size distribution shown in figure 3,

459   which are used in the present analysis.

460

461   In figure 4c the peak value for a_r =110 µm and this is based on the value of d_{b50} for the bed

462   sediments shown in figure 3. Since the bed sediments have a d_{b50}=320 µm, then if all the bed

463   sediments were entrained the suspended d_{50} would be 320 µm and as noted above for δ=0.4, a_{bc}=

464   d_{b50}/2.9, therefore it follows the maximum value for a_r will be 110 µm. However, the condition

465   for all size fractions being entrained occurs only during the most energetic events and in general,

466   as shown in figure 4c, the suspended sediments have a size fraction which is smaller than the bed

467   and this reduces with height above the bed following the form shown in figure 4b and given by

468   equation (12b). This size sorting has implications for the acoustic inversions to be discussed.

469

470   *3.2 The forward problem; calculating the backscattered signal for the inversions.*

471

472   Using the suspended sediment time series presented in figures 4a and 4d, with the specified

473   lognormal distribution for n(a) presented in figure 3, the forward problem of propagating sound

474   through the suspension field was solved using equation (A1.4) in Appendix 1 and the

475   backscattered signal calculated. Firstly backscatter signals were calculated with no uncertainties.

476   Secondly, systematic errors and random fluctuations were introduced into the backscattered

477   signal via equation (A1.4), due to variability in the scattering characteristics $K=\varepsilon K(1\pm\gamma_s)$ and

478    $\xi=\varepsilon\xi(1\pm\gamma_s)$, the statistical nature of the backscattered signal $V_{rms}=V_{rms}(1\pm\gamma_v)$ and calibration

479   uncertainties $\Re=\varepsilon\Re(1\pm\gamma_\Re)$. ε was a scaling factor either greater or less than unity and

480   independent of range from the transducer and time. γ_s, γ_v and $\gamma_\Re$ had random values with range

481   and time, that lay between 0-γ_o and were uncorrelated between the parameters. When a multi-

482   frequency system was simulated the random components were also uncorrelated between

483   frequencies. The time averaged value for the random components was zero. The lack of a

484   systematic error for V_{rms} was because this was introduced through $\Re$. These computed

485   backscattered signals were used in different inversion scenarios based on equation (1) and its

486   simplification and the calculated acoustic estimates for the concentration, M, and particle radius,

487   a_M, compared with C and a_c shown in figure 4.

488

4. INVERSION SCENARIOS

489

490 In this section a number of inversions scenarios of increasing complexity are described. These
491 are broadly in terms of the type of ABS used, whether it be single or multi-frequency, the
492 underlying assumptions made regarding the suspension structure, how supporting independent
493 data can be used to aid the acoustic inversions and an assessment of the impact systematic and
494 random errors have on the acoustic estimates of a_c and C. Tables 1 and 2 provide an overview of
495 the conditions for all the cases simulated which are outlined below. In Section 5, the calculated
496 acoustic values for M and a_M for the varying scenarios are presented.

497

498 *4.1. Single frequency, SF, cases; SF1, SF2, SF3 in table 1*

499

500 For the first three cases named SF1, SF2 and SF3 in table 1, a single frequency ABS operating at
501 2 MHz mounted at 1.0 m above the bed with a vertical spatial resolution of 0.005m was
502 examined. Systematic, ε, and random, γ_o, uncertainties were introduced into the forward
503 calculation through equation (A1.4) and in the inversions assumptions were made about the
504 suspended particle size, the effect of acoustic attenuation and the transducer nearfield directivity.
505 Since a single frequency was employed these inversions only calculated profiles of suspended
506 mass concentration, M, for the conditions described in section 3.1.

507

508 Case SF1 corresponds to a practical situation where only the d_{b50} value of the bed sediments was
509 known. The inversion was therefore evaluated using $a_o = d_{b50}/2$ (160 μm), the intrinsic functions
510 for K_i and ξ_i and with no grain size sorting with height above the bed and in time. The
511 concentration profiles for M were calculated for three inversions scenarios. SF1a where no
512 uncertainties were introduced into the forward calculation of the backscattered signal, ε=1, γ_o=0
513 and in the inversion sediment attenuation was assumed negligible, $r\alpha_s \ll 1$, and the nearfield
514 correction was ignored, ψ=1. SF1b where uncertainties, ε=0.8 and ε=1.2 and γ_o=0.1 were
515 introduced into the calculation of the backscattered signal and again in the inversion it was
516 assumed $r\alpha_s \ll 1$ and ψ=1. SF1c with no uncertainties, ε=1 and γ_o=0, being used in the calculation
517 for the backscattered signal, and with α_s and ψ being accounted for in the inversion. In this latter
518 case, the iterative implicit inversion had to be applied for the calculation of M profiles.

519   In the case SF2, further sediment size information was available in the form of a bed sample.

520   The inversion was therefore evaluated using the lognormal number density distribution function

521   of the bed, $n_b(a)$, to calculate the ensemble mean values of the sediment parameters, $a_o=a_{bc}$ (110

522   μm), K and ξ with no grain size sorting with height above the bed and in time. The concentration

523   profile M was calculated for three inversion scenarios named SF2a, SF2b, SF2c which were the

524   same in terms of uncertainty, attenuation and nearfield conditions to scenarios SF1a, SF1b and

525   SF1c. For the third case, SF3, some information on the suspended sediments was considered

526   available. This case simulates the situation when samples of the suspended sediments were

527   collected or an assumption was made for the time averaged suspended size profile based on the

528   bed sediments. In the latter case $a_o=a_{bc}(z/z_r)^{-l}$, $l=0.2$, and K and ξ were a function of height above

529   the bed, z, however, they were still time invariant. The same three scenarios of uncertainty,

530   attenuation and nearfield conditions for SF1, SF2 were applied to case SF3.

531

532   *4.2. Multi-frequency, MF, cases; MF1, MF2, MF3 in table 2*

533

534   The utilisation of a multi-frequency ABS system provides the opportunity to estimate vertical

535   profiles of both the M and a_M as a function of time. For the cases studied here the ABS had

536   frequencies of 0.7, 1.25 and 3.0 MHz, was mounted 1m above the bed and had a vertical

537   resolution of 0.005 m To carry out the multi-frequency inversion requires an estimate for the

538   form of n(a) so that K and ξ can be calculated in the inversion. n(a) was chosen to be the same as

539   in the forward calculations based on the bed lognormal sediments size distribution shown in

540   figure 3 with $σ=0.4a_o$. To obtain the acoustic estimates for a_c, in the inversion a_M was obtained

541   from values of a_o covering the range 5-400 μm with a step interval of $δa=2$ μm.

542   In the first multi-frequency case, MF1, no uncertainties were introduced into the forward

543   calculation, $ε=1$ and $γ_o=0$. To simplify the inversion an assumption that sediment attenuation

544   could be ignored, $rα_s«1$, led to an explicit solution, further the nearfield correction was ignored,

545    $ψ=1$. In the second case of multi-frequency scenarios, MF2, a more complex implicit iterative

546   inversion was used with $α_s$ accounted for and the nearfield correction applied. In MF2 systematic

547   and random errors were added to the forward calculations of the backscattered signal in the

548   evaluation of equation A1.4 and different conditions of uncertainty were examined. As presented

549   in Table 2, in scenarios MF2a, $\varepsilon=1$ and $\gamma_o=0$, in MF2b, $\varepsilon=0.8$, 1.2 and $\gamma_o=0$, and in MF2c, $\varepsilon=0.8$,

550   1.2 and $\gamma_o=0.1$. In the third case MF3, the time series profiles of a_M from MF2c were averaged to

551   give a temporal mean average profile, $\overline{a_M}$, and for the same conditions as MF2a and MF2c the

552   profiles for M were re-calculated using $\overline{a_M}$. This latter calculation was carried out because the

553   impact of both ε and γ_o on $\overline{a_M}$ was relatively weak as will be shown in the following section.

554

555 **5. ACOUSTIC ESTIMATES FOR PARTICLE SIZE AND CONCENTRATION**

556 In this section the inversion scenarios described in Section 4 are implemented and the results

557 examined in terms of the accuracy of the acoustic estimates of the suspended particle size and

558 concentration. Having a priori knowledge of the suspension can improve the inversion and using

559 more sophisticated inversions can provide further information on the suspension. For the first

560 three inversion cases SF1, SF2 and SF3, a single frequency ABS was assessed with parameter

561 uncertainties and assumptions made about the suspension as described in Section 4.1 and Table

562 1. These inversions only calculated profiles of M. Following these cases, three cases of multi-

563 frequency ABS deployments, MF1, MF2 and MF3, were examined with parameter uncertainties

564 and assumptions made about the suspension as described in Section 4.2 and Table 2. In these

565 inversions profiles of a_M and M were obtained. Following the inversion scenarios, further

566 calculations are reported to assess the impact of uncertainties on the profiles of a_M and M.

567

568 *5.1 Estimates of suspended sediment concentration, M, using single frequency ABS for cases*

569 *SF1, SF2 and SF3 given in Table 1*

570 The backscatter signal from suspended sediments is a function of the particle size and

571 concentration. If an estimate of the suspended size is available then a single frequency ABS can

572 be used to obtain a measurement of the concentration field. Using the suspension field shown in

573 figure 4 the backscattered sound field was computed as described in Section 3.2 using equation

574 A.4.1 ABS systems usually operate over the range 0.5-5.0 MHz and for the present simulations

575 the frequency was chosen to be 2.0 MHz. From the previous section the bed sediment particle

576 size was given a value of d_{b50}=320 μm (a_o=a_{bc}=110 μm), which gives x_o=0.93 at 2.0 MHz and

577 places the scattering above the Rayleigh regime x<<1 and below the geometrical regime x>>1.

578 Backscattering in the intermediate regime has a lower sensitivity to changes in particle size than

579 in the Rayleigh regime and sediment attenuation is not as significant as it is at higher

580 frequencies; the lower sensitivity to size and attenuation contributes to reducing inversion errors.

581 The 2 MHz single frequency ABS was mounted at 1.0 m above the bed and had a vertical spatial

582 resolution of 0.005m.

583

584   The conditions for the different cases with their scenarios are presented in Table 1. For the first

585   single frequency case SF1, the simple situation of a single frequency 2.0 MHz ABS deployment

586   was considered. The only information available for the local site was an estimate for d_{50} of the

587   bed which was 320 μm. To obtain the suspended concentration the explicit solution of equation

588   (4) was used, ie $r\alpha_s \ll 1$, $\psi=1$ and it was assumed $\mathfrak{R}$ had previously been measured. As no

589   information was available for m(a), K_i was obtained using the intrinsic value for $f_i/\sqrt{\rho}$

590   calculated using the expression in equation (3a) for a particle radius of $a_o=d_{50}/2$. The value for K_i

591   was constant over time and height above the bed. The results for this straightforward inversion

592   are shown in figure 5. Firstly the inverted computed concentration field, M, obtained using

593   backscattered signals without added uncertainties, $\varepsilon=1$, $\gamma=0$, scenario SF1a, is presented in figure

594   5a. The impact of not accounting for the nearfield is observed between z=0.9-1.0 m where the

595   concentration field reduces rapidly. Apart from this nearfield artifact, it can be seen that the

596   temporal structure of the suspension field in figure 5a is comparable with that of figure 4d,

597   although the magnitude in figure 5a is decreasing at a greater rate with z. This is illustrated in

598   figures 5b and 5c in which the concentration from the inversion, M, is centered on the solid

599   circles, scenario SF1a, with a shaded area bound by inversions associated with systematic errors

600    $\varepsilon=0.8$ and 1.2, and random errors $\gamma_o=0.1$ scenario SF1b, and the solid line is from the input

601   concentration field, C, at the same value of z. The upper boundary of the shaded area is

602   associated with scattering and calibration characteristics that are greater than those assumed for

603   the inversion, i.e. $\varepsilon=1.2$, while the lower boundary is associated with reduced scattering and

604   calibration characteristics than assumed in the inversion, i.e. $\varepsilon=0.8$. The two heights shown are at

605   the reference height $z_r=0.005$ m and z=0.9 m. It can clearly be seen that at z_r, M is similar in

606   form and magnitude to C_r. That the magnitudes are comparable may be somewhat surprising,

607   given K_i and $d_{b50}/2$ where used for the inversion, however, coincidentally, $K_i=1.43$ for $d_{b50}/2$ and

608   K=1.73 for a_{cb} at 2.0 MHz at z_r, hence their values are similar and therefore M is a reasonably

609   accurate estimate. At z=0.9 m the temporal structure of M is still comparable with C, however,

610   the magnitude of M is an order of magnitude smaller. This reduction is due to assuming $a_o=d_{50}/2$

611   in the inversion, while the actual temporal mean value, $\bar{a}_c$, at 0.9 m was 29 μm, which has

612   associated lower scattering characteristic. The general trend of increasing departure of M from C

613   with height above the bed is shown by the temporal mean concentration profiles in figure 5d.

614   The dashed line in figure 5d is an implicit iterative inversion using equation (7) in which the

615   nearfield and sediment attenuation were accounted for, scenario SF1c. As can be seen there is

616   only a marginal increase in $\overline{M}$. Therefore using K_i and $d_{50}/2$ in the inversion provides a temporal

617   structure for M which is comparable with C, but with M becoming increasingly erroneous in

618   magnitude with z. The temporal-spatial mean value for $\overline{M/C}$=0.23; including the nearfield

619   correction and sediment attenuation only increased this value to $\overline{M/C}$=0.25. The suspended

620   concentration field was therefore significantly underestimated for all SF1 scenarios.

621

622   In the second single frequency case, SF2, the assumption was made that bed samples from the

623   location site were available. Using the samples the 2.0 MHz ABS could be calibrated for the site

624   specific suspension in the laboratory and $K\Re$ obtained, or if $\Re$ is known, n(a), a_o, f and hence K

625   could be estimated from the bed samples using equations (2a, 2c, 3a). Either way the inversion

626   was carried out assuming a suspension with $n_b(a)$ (i.e. identical to that of the bed) and invariant

627   with time and height above the bed. The results for such an inversion are shown in figure 6

628   where the same nomenclature as used in figure 5 is employed. Figure 6a, represents the result for

629   scenario SF2a. The results of scanarios SF2a, SF2b and SF2c are shown in figures 6b-6d.

630   Although expectations may have been for improved agreement between M and C, as noted

631   earlier the values for K and K_i at 2.0 MHz used in the inversions to obtain figures 5 and 6 were

632   within 20% of one another, with the result that the profiles for M in the two figures are very

633   comparable. In figure 6b at the high concentration events, when the nearbed suspended

634   sediments have a value of a_o equal to that of the bed, the results for M still underestimate C_r, due

635   to the assumption that $r\alpha_s\ll1$. Overall the resulting M profiles in figure 6 have essentially the

636   same problem as in figure 5, the lack of accounting for the particle size sorting with z again

637   results in an increasing underestimate of the suspended concentration with height above the bed.

638

639   Owing to the lack of agreement between M and C with z for inversion cases SF1 and SF2 seen in

640   figures 5 and 6, in the third case, SF3, particle size sorting with height above the bed was

641   included in the inversion. Obtaining suspended sediment samples at the deployment site could be

642   used to estimate the sorting, or bed samples could again be used, but combined with an estimate

643   for the temporal mean particle radius profile, $\overline{a_o(z)}$, with height above the bed. In the present

644   scenario the latter option was used with $\overline{a_o}=a_{bc}=110$ μm at z_r and with a reduction in mean

645   particle size with height above the bed given by equation (12b). Therefore using the size profile,

646 K was calculated at each height above the bed and a time invariant profile for K obtained. The

647 results from this inversion for scenarios SF3a and SF3b are shown in figures 7a-7c. As would be

648 expected, given the results in figures 5 and 6, using a profile size estimate in the inversion results

649 in a substantial improvement in the agreement between M and C with z. Both the temporal

650 structure and the magnitude of M agree reasonably well with C at all elevations above the bed,

651 with a temporal-spatial mean value, $\overline{M/C}$=0.54, which is a significant improvement over the two

652 previous cases, SF1 and SF2. Again accounting for the nearfield and sediment attenuation in

653 scenario SF3c, shown in figure 7d, obtained using equation (7) only provides a marginal

654 improvement with $\overline{M/C}$ increasing to 0.58.

655

656 The reason why in SF3c the value of M is still an underestimate is because the particle size

657 profile is based on a reference value at z_r of $\overline{a_o}=a_{bc}$ for the bed and this represents the maximum

658 one would expect to obtain as a reference. In practice this value is only achieved for the most

659 dynamic conditions as illustrated in figure 4c. Therefore in figures 7b and 7c the values for M

660 and C are only coincident for the more energetic events and in general M underestimates C

661 because the particle size is overestimated. Furthermore, as shown in figure 7b for scenario SF3b,

662 even though the correct value for a_o is being employed at z_r for the more energetic events, the use

663 of $r\alpha_s$«1 results in the concentration during these events being underestimated. Therefore the

664 inclusion of a representative size profile provides a significant improvement in the acoustic

665 estimate of the suspended concentration profile, however, because the size profile is invariant

666 with time and based on the particle size distribution of the bed, it still fails to capture the exact

667 nature of the suspended concentration field. To do this an inversion needs to be carried out which

668 contains information on the time variability of the suspended particle size field. One way of

669 doing this is to use multi-frequency acoustics to also measure particle size.

670

671 *5.2 Estimates of suspended sediment particle size, a_M, and concentration, M, using multi-*

672 *frequency ABS for cases MF1, MF2 and MF3given in Table 2*

673 If particle size as well as concentration is desired, then multiple frequencies are employed and

674 the differential scattering characteristics with frequency of the sediment in suspension is utilised

675 to calculate profiles of the time varying particle size and concentration. In the present study

676 inversions were carried over the range a_o=2-400 µm with a step interval of 2 µm and a_M and M

677 obtained at the minimum value of Φ as expressed by equation (8). This range of radii covers the

678 Wentworth grain size scale from fine silt through to coarse sand. A simple approach would be to

679 add only one acoustic frequency to the single frequency system described above, however the

680 lack of uniqueness in the value of K with particle size makes the inversion problematic; with

681 erroneous results readily generated; this is illustrated in Appendix 3. Most publications using

682 multi-frequency ABS have therefore opted for a three frequency system (Crawford and Hay,

683 1993; Thorne and Hardcastle, 1997; Thosteson and Hanes, 1998; Villard et al, 2000 and

684 Smerdon et al 2007) and it is such a system which is investigated here. Typically ABS have been

685 deployed in sandy environments and operated in the 0.5-5 MHz frequency range. At much lower

686 frequencies scattering is in the Rayleigh region, x<<1, where backscattering can be weak and at

687 much higher frequencies the combined water and suspended sediment attenuation both reduce

688 the backscattered signal level and introduce instabilities into the inversion (Thorne et al, 1995).

689 With regard to the above, the present study examines scenarios for an ABS operating at 0.7, 1.25

690 and 3.0 MHz in a sandy environment. As with the 2 MHz single frequency ABS the system was

691 mounted at 1.0 m, above the bed and had a vertical spatial resolution of 0.005m.

692

693 All the multi-frequency inversions were carried out with a lognormal n(a) having $\sigma=0.4a_o$, which

694 gave them a value for the normalized standard deviation, δ, that was the same as the bed and the

695 a_c field. The conditions for the different cases with their scenarios are presented in Table 2. The

696 first inversion for case MF1 yielding M and a_M was carried out using equations (2a), (3a), (4) and

697 (8). No uncertainties were introduced into equation (A1.4) for the forward calculation of the

698 backscattered signal, $\varepsilon=1$ and $\gamma_o=0$. For the inversion α_s was assumed negligible and no nearfield

699 correction applied, therefore any deviations between the suspension field, C and a_c, and the

700 acoustic estimates, M and a_M, was solely due to the simplification of assuming $r\alpha_s \ll 1$ and $\psi=1$.

701 Table 2, case MF1, provides an overview of the inversion condition with the outcome from this

702 inversion being shown in figure 8. As seen in the mean temporal profiles shown in figures 8a and

703 8b, the impact of ignoring the nearfield for each transducer produces a local effect close to the

704 ABS, with the particle size over estimated and the concentration underestimated. Between

705 approximately z=0.2-0.8 m the mean profiles of a_M and M from the ABS are consistent with the

706 suspension field. However, below z=0.2m the ABS inversion increasingly overestimates the

707 particle size and underestimates the concentration. As can be seen in figures 8c and 8d the

708   general temporal-spatial form of the suspension field is retained in the inversion, although, as

709   shown in figures 8e and 8f, close to the bed during the higher suspension events, the lack of

710   accounting for sediment attenuation in the inversion, leads to significant overestimates of particle

711   size and underestimates of concentration. Overestimates of a_r by a factor of two and

712   underestimates of C_r by a factor of five occurred during the most dynamic suspension events.

713   Therefore neglecting attenuation, when using a multi-frequency ABS, to extract particle size and

714   concentration, can be problematic and this is particularly acute at the more interesting near bed

715   higher concentration events.

716

717   In the second multi-frequency case, MF2, the forward calculation for the backscattered signal

718   had uncertainty conditions of $\varepsilon=1.0$ and $\gamma_o=0$, MF2a, $\varepsilon=0.8$, 1.2 and $\gamma_o=0$, MF2b, and $\varepsilon=0.8$, 1.2

719   and $\gamma_o=0.1$, MF2c; again these scenarios are summarised in Table 2. For this case a full inversion

720   using equation (1-3, 6-8) was employed with account taken of α_s and ψ. Figures 9 and 10

721   respectively show the results for the acoustic estimates of particle size, a_M, and concentration, M.

722

723   In figure 9a, the time averaged particle radius profiles, $\overline{a_M}$, with regions of uncertainty and $\overline{a_c}$ are

724   shown. The shaded red and blue regions show the envelopes of the bounded inversion results for

725   the uncertainty conditions MF2b and MF2c respectively. The solid line is the $\overline{a_c}$ profile and the

726   solid circles the $\overline{a_M}$, profile for MF2a. The temporal averaged results from the inversions show

727   that $\overline{a_M}$ is consistent in form to $\overline{a_c}$ with z, with the region of uncertainty increasing as the height

728   above the bed is reduced. In figure 9a the two regions of uncertainty (red and blue) overlapped

729   considerable. In figures 9b and 9c are respectively shown a_M for $\varepsilon=1.2$, $\gamma_o=0.1$ and $\varepsilon=0.8$, $\gamma_o=0.1$,

730   correspond to inversion scenarios MF2c in Table 2. As can be seen in the figures the broad

731   temporal structure of a_M is comparable to that shown in figure 4a for a_c, although somewhat

732   noisier owing to the introduction of random errors into the backscatter calculation. Analysis of

733   the inversion shows that close to the bed for $\varepsilon>1$ $a_M<a_c$ and for $\varepsilon<1$ $a_M>a_c$, as illustrated by the

734   colour bar scales in figures 9b and 9c. In figures 9d and 9e the temporal variability is highlighted

735   more clearly at the reference height and at z=0.9 m. The nomenclature for these figures is the

736   same as for figure 9a; the solid line is a_c, the solid circles MF2a and the red and blue shaded

737   areas are respectively MF2b and MF2c. Figure 9d shows the results at z_r for MF2b, $\gamma_o=0$, red

738   shaded area, and good estimates for a_M were obtained when the concentrations were relatively

739   low, however, at the higher concentrations the region of uncertainty is large. This is due to

740   positive feedback arising from the implicit iterative inversion when sediment attenuation

741   becomes significant (Thorne et al 2011b) and errors propagate and increase with range from the

742   transducer. For the scenario where when $\gamma_o=0.1$, blue shaded area, MF2c, the introduction of a

743   random component uncorrelated at each frequency, introduces further variability into the

744   estimate of a_M which can be significant. In figure 9e for the scenario MF2b, $\gamma_o=0$ at z=0.9 m,

745   corresponding to the red shaded area, the time series for a_M is almost identical to that of a_c. This

746   arises due to the manner in which a_M was obtained from the minimum of Φ using equation (8),

747   where changes in ε have a similar impact on $\sigma_m(a_o)$ and $M(a_o)$ when sediment attenuation is not

748   significant. Therefore, there is only a marginal impact on Φ and hence the values of a_M. For the

749   scenario MF2c, when $\gamma_o=0.1$, corresponding to the blue shaded area in figure 9e, the gross

750   underlying structure of the time series is present, however, the introduction of a random

751   component uncorrelated at each frequency, introduces variability into the temporal estimate of

752   a_M which can be significant.

753

754   In figure 10 the inversion output for M is shown using the same nomenclature as figure 9 and for

755   the same case MF2. In figure 10a, the time averaged concentration profile, $\overline{M}$, with regions of

756   uncertainty corresponding to scenarios MF2a, MF2b and MF2c are presented with $\overline{C}$. As with $\overline{a_M}$

757   and a_c, it can be seen that the results for $\overline{M}$ are similar in form to $\overline{C}$ with height above the bed and

758   with the region of uncertainty increasing towards the bed, although this region of uncertainty is

759   significantly greater than for the case of $\overline{a_M}$. In figures 10b and 10c are respectively shown M for

760    $\varepsilon=1.2$, $\gamma_o=0.1$ and $\varepsilon=0.8$, $\gamma_o=0.1$, corresponding to inversion scenario MF2c In the figures it can

761   be observed that the general pattern in the suspended sediment concentration is broadly

762   consistent with those of C shown in figure 4d. Results from the inversion shows that when $\varepsilon>1$

763   M>C and when $\varepsilon<1$ M<C, as indicated by the colour bar scales in figures 10b and 10c. In figure

764   10d is shown the time series of M at z_r. For the scenario MF2b, red shaded area, the periods of

765   lower concentration yield values of M comparable to C_r, however, at the higher concentration

766   events the values for M are substantially overestimated for $\varepsilon=1.2$ and underestimated for $\varepsilon=0.8$.

767   As with a_M, these substantial uncertainties just above the bed at high concentration events are

768   due to the multi-frequency coupled errors propagating with range when attenuation becomes

769   significant. For the MF2c scenario, blue shaded area, the addition of the random noise

770   component generates further uncertainties. In 10e is shown the time series for M at 0.9 m above

771   the bed, for the case MF2b when $\gamma_o=0$, the region of uncertainty in M closely follows C, with M

772   marginally overestimating C when $\varepsilon=1.2$ and underestimating when $\varepsilon=0.8$. The addition of the

773   random noise component, MF2c, with $\gamma_o=0.1$, can add significant variability to M.

774

775   The fluctuations in a_M associated with the random component, γ_o, has a significant impact on the

776   temporally estimated values of M. However the random component reduces towards zero with

777   temporal averaging. Therefore if a lower temporal resolution for a_M is acceptable improved

778   estimates for M can be obtained. Using the three $\overline{a_M}$ profiles shown in figure 9a, obtained from

779   the MF2a, $\varepsilon=1$ and $\gamma_o=0$, and MF2c, $\varepsilon=0.8$, $\gamma_o=0.1$ and 1.2, $\gamma_o=0.1$ scenarios, M was re-calculated

780   for scenario MF3a and MF3b. This resulted in the new values for M shown in figure 11. The

781   mean profile of M for $\varepsilon=1$ and $\gamma_o=0$, MF3a, is given by the solid circles, with the region of

782   uncertainty, represented by the grey shaded area bounded by $\varepsilon=0.8$, 1.2 and $\gamma_o=0.1$, MF3b, is

783   shown in figure 11a and is seen to be comparable with figure 10a. The temporal structure of M

784   shown in figures 11b and 11c respectively for $\varepsilon=1.2$ and $\varepsilon=0.8$ each with $\gamma_o=0.1$, are somewhat

785   less noisy than figures 10b and 10c, due to the use of $\overline{a_M}$, and more consistent with figure 4d.

786   However, it is in the detailed times series illustrated by the results at z_r and z=0.9m respectively

787   in figures 11d and 11e that show clear improvements over figure 10 in the values and

788   uncertainties in M. Therefore by reducing the variability in a_M due to random uncertainties,

789   through forming a temporally averaged profile, $\overline{a_M}$, from the output from a multi-frequency

790   iterative implicit inversion, it is possible to reduce uncertainties and improve the accuracy of the

791   high temporal-spatial re-calculated values of M. However, because a mean profile for a_M is being

792   utilized, it is not possible to fully capture the exact variation in C, as illustrated in figure 11d and

793   11e. Although not presented for brevity, similar results to those shown in figure 11 were also

794   obtained using multi-frequency temporally averaged $\overline{V_m^2}$ to obtain $\overline{a_M}$ and again using $\overline{a_M}$ for the

795   high spatial-temporal inversion for M.

796

797   *5.3 Sensitivity analysis and error estimations as a function of uncertainty*

798

799   The inversion outcomes in figures 9-11 provide a specific illustration of the impact on a_M and M

800   of systematic and random variability in the backscattered signal. To obtain a broader assessment

801   of the impact of uncertainties the backscattered signal was calculated over a range of values for ε

802   and γ_o and full iterative implicit inversions carried out accounting for α_s and ψ using equations

803   (1-3,6-8). The suspension field in figure 4 was again used and backscatter signals calculated as;

804   (i) the systematic error ε, increased from 0.5-1.5 with $\gamma_o=0$ and (ii) the range of variation of the

805   independent random errors increased as γ_o changed from 0.0-0.2 with $\varepsilon=1$. The first case in

806   figure 12a shows the temporal-spatial mean values for $\overline{a_M/a_c}$ and $\overline{M/C}$ with error bars derived

807   from the standard deviation of the ratios. The results show that $\overline{a_M/a_c} \approx 1$ and as previously

808   mentioned this arises due to changes in ε having a similar impact on $\sigma_M(a_o)$ and $M(a_o)$ and hence

809   Φ and therefore only marginally impacting on the values of a_M. The values for $\overline{M/C}$ are

810   somewhat different and shows that when the scattering and calibration characteristics are lower

811   than assumed in the inversion, $\varepsilon<1$, the value for M significantly underestimates C and if $\varepsilon>1$

812   then M is substantially greater than C. This is consistent with the observations made for the SF

813   cases when a_o was assumed and only M was being estimated. In general, however, it is unlikely

814   that uncertainties would apply exactly equally at each frequency, therefore the second case looks

815   at the impact of random variability; this is shown in figures 12b and 12c. In figure 12b it can be

816   observed that $\overline{a_M/a_c}$ marginally increased with γ_o, however, the standard deviation steadily

817   increased reaching a standard deviation of around $\pm50\%$ for $\gamma=0.2$. In figure 12c the results for

818    $\overline{M/C}$ are shown by the solid circles and the form is quite different to that of $\overline{a_M/a_c}$ with both

819    $\overline{M/C}$ and the error bars increasing substantially above $\gamma_o \approx 0.05$. This substantial increase is

820   associated with the dependence of M on a_o through K. As illustrated in figure 1, when $x<1$, the

821   dependency of M on a_o tends to a_o^3, therefore errors in the realizations of a_M which reduce

822   estimated particle size have a substantial impact on the computed variability of M. Also when

823   realizations result in increases in a_M, then owing to the dependency of M on a_o being weaker for

824    $x\geq1$, there is a resulting bias in $\overline{M/C}$ leading to values increasingly becoming greater than unity

825   as γ_o increases. This impact varies with mean particle size (Moate and Thorne, 2009), decreasing

826   as mean particle size increases as shown in appendix 4. If the data used to obtain figure 12b, is

827   employed to provide $\overline{a_M}$ profiles for each value of γ_o, and the inversions repeated using $\overline{a_M}$ then

828   the results shown by the open circles in figure 12c are obtained. The impact of the uncertainties

829   is substantially reduced with $\overline{M/C}$ remaining close to unity and error bars being approximately

830   constant. Figure 12 illustrates in broad terms the impact on the calculated values for a_M and M

831   that variations in the backscattered signal have on the output of the inversion. For accurate

832   inversions of a_M and M, precise knowledge of n(a), K, ξ and $\Re$ are required and increasing so as

833   particle size reduces, although results for M can be significantly improved using $\overline{a_M}$ in the

834   calculation due to the nominally unbiased estimates of $\overline{a_M}$.

835

836   *5.4 Relationship between the a_M and d_{50}*

837   It was remarked in section *3.1,* that the acoustic size, obtained from inverting the backscattered

838   signal, is not the median mass diameter, d_{50}, used almost universally in sediment transport

839   models to define the size of the sediments in suspension. The acoustic measurement of particle

840   diameter, $d_M=2a_M$, derived using a range of a_o, given by equation 2(c), is an estimate for $2a_c$ and

841   is based on a probability density function representing the number of particles with size, n(a),

842   rather than the mass of the particles with size, m(a). If the assumption is made that the particles

843   are nominally spherical in shape then n(a) is obtained from $m(a)/a^3$. Using this relationship the

844   variation of d_{50}/d_M, with the normalised standard deviation, $\delta=\sigma_m/a_m$, can be calculated for

845   lognormal and normal mass distributions. The results are shown in figure 13, with the open

846   circles and crosses respectively representing the value for d_M calculated using $m(a)/a^3$ and the

847   solid circles and solid triangle representing d_M calculated using a full acoustic iterative implicit

848   inversion of the backscattered signal with equations (1-3,6-8) using forward scattered fields

849   based on $\overline{a_c}$, and $\overline{C}$. For the lognormal mass distribution it can readily be observed that as δ

850   increases the value for d_{50}/d_M accordingly becomes larger and is moderately well represented by

851   an expression of the form

852
$$d_{50} = d_M e^{(1.4\delta)^{1.7}} \tag{13}$$

853   This relationship allows d_{50} to be readily obtained from the acoustically measured value of d_M.

854   For the case of a normal mass distribution the same expression is applicable for $\delta \leq 0.1$, however,

855   above this value d_{50}/d_M steeply rises due to the rapid increase in the small particles in the n(a)

856   distribution derived from the m(a). Hence the small size tail of a normal mass distribution can

857   have a significant effect on the acoustically estimated size and therefore care must be taken when

858   applying a normal distribution fit to measured mass size distributions to ensure the fine fraction

859   of the suspended sediment are actually of this form. In general, if sediment samples are available,

860   it may be more prudent to convert the measured mass in each size range to a particle number

861   distribution and then apply the measured n(a) in equation (2). It would then be necessary to

862   convert the acoustically measure d_M to d_{50} by forming a curve similar to that presented in figure

863   13 to calculate d_{50}.

864

6. DISCUSSION AND CONCLUSION

As commercial instruments have become available the application of acoustic backscatter systems, ABS, to the measurement of particle size and concentration has steadily increased in use over the past two decades. The majority of users of ABS have a limited background in acoustics and therefore obtaining suspended sediment parameters from ABS data can on occasions prove to be somewhat problematic. The aim of the present work has therefore been to provide an overview and assessment, of the methodology commonly used to extract suspended sediment parameters, from backscattered acoustic data collected over mobile beds of inorganic non-cohesive sediments at normally employed low megahertz ABS frequencies.

The focus of the study has been on the inversion of ABS data to obtain suspension profiles, with a précis on the forward problem for calculating the backscattered signal in Appendix I. Equations (1-3,6-8) provide the general solution for estimating suspended sediment concentration profiles; this solution is an implicit expression in M, it is solved iteratively and progressively with range along the direction of sound propagation, and requires a methodology to simultaneous obtain a_M if particle is size unknown. This solution can be considerably simplified if sediment attenuation can be ignored, $r\alpha_s \ll 1$, an estimate for the suspended particle size is available, and interest is in the transducer farfield. This resulted in equation (4), where after accounting for α_w, M at any range is simply proportional to V_m^2. This solution has the benefit of simplicity, requiring only a single frequency ABS. However, it is restricted to the farfield, the assumption $r\alpha_s \ll 1$ and particle size is invariant with height and time above the bed. The restriction of only transducer farfield scattering can readily be addressed using the nearfield expression of Downing et al (1995) and α_s can be evaluated using equation (2b) and applying the iterative formulations given in equations (6) and (7). This inversion therefore still only requires a single frequency ABS and the inversion is reasonably straight forward, although it is subject to a constant particle size with z and time. If the requirement is to obtain time series profiles of a_M and M, then multi-frequency ABS is required and the systems adopted generally use three frequencies. The use of three rather than two frequencies helps to stabilise the inversion. The extraction of a_M from multi-frequency backscatter data increases the complexity and computation time of the acoustic inversions as described in equation (8) and the inversion becomes increasingly time consuming when α_s is significant. Further to carry out the inversion for a_M an estimate for n(a) is required, since, as

896   show in figure 1, the suspension scattering characteristic are impacted by having a range of
897   particle sizes in suspension. The extraction of a_M and M from a multi-frequency ABS therefore
898   requires a greater level of understanding of the interaction of sound with suspended sediments
899   than when only M is required.

900

901   The backscattered signal, V_m^2, used in the inversion, to calculate M or M and a_M, requires the
902   calculation of an average value from an ensemble of independent backscattered signals. This
903   arises because of the statistical nature of the scattered signal which leads to $\sigma_e(V_m^2)/V_m^2=1/\sqrt{\eta}$,
904   where η is the number of independent samples. In the present study the reduction of the
905   autocorrelation function of the backscattered signal has been used to assess the independence of
906   samples and this led to a time interval of around 5 ms for independent samples. The 5 ms time
907   interval provided a nominal value for independent samples, although this will vary depending on
908   frequency and the intensity of the flow turbulence. In rough turbulent flows, the root-mean-
909   square turbulent horizontal velocity, $\sqrt{\overline{u'^2}}$, is around   15-20% of the mean velocity, u_o,
910   (Heathershaw 1976) and decorrelation can be considered to occur when the relative movement of
911   the particles is greater than $\lambda/4$, therefore an estimate for τ_o may be $\tau_o \approx \lambda/u_o$. The limitation on
912   the time interval between independent samples leads to a tradeoff between spatial-temporal
913   resolution and the accuracy of the estimated values for a_M and M.

914

915   To investigate the acoustic estimates of a_M and M a suspension field was generated. The field
916   was constructed so that it had a vertical time-averaged sediment concentration profile
917   corresponding to the well-known Rouse profile. In the absence of a general theory for vertical
918   size sorting, the imposed vertical sediment size formulation was chosen on the basis of previous
919   observations obtained by Thorne et al. 2011a over rippled beds. Although in practice the validity
920   of this mean size sorting formulation is not guaranteed and vertical temporal differential settling
921   velocities were not rigorously specified, the simulated suspension field offered the opportunity to
922   assess inversions when size sorting effects are present.

923

924   Using the representative suspension field, the forward problem of propagating sound through the
925   suspension was computed and the backscattered signal obtained. Different backscattered signals
926   were calculated to account for uncertainties in; (i) the system calibration, (ii) the formulated

927 scattering characteristics and (iii) the scattering statistics. This variability in the backscattered
928 signal provided the opportunity to assess the impact of uncertainty on the calculated profiles of
929 a_M and M. To examine the estimated values for a_M and M a number of scenarios were
930 considered, in the first instance only M was obtained from the inversion and this was followed
931 by a_M and M. Three cases SF1, SF2 and SF3, were considered for the inversion of M based on a
932 single frequency 2.0 MHz ABS. The outcome from these inversions were presented in figures 5-
933 7 and show that the temporal structure of M remained consistent with C, however, the values for
934 M reduced with height at a greater rate than C, owing to the lack of accounting for size sorting.
935 The main factor for improving agreement between M and C in these scenarios was to obtain an
936 estimate for the variation in a_c with height above the bed and use this in the inversions.

937

938 Following on from the 2.0 MHz studies three cases, MF1, MF2 and MF3, were carried out for
939 calculating a_M and M using a multi-frequency ABS inversion at 0.7, 1.25 and 3.0 MHz . The first
940 focused on an inversion neglecting α_s and setting $\psi=1$. The results in figure 8 showed that using
941 $\psi=1$ introduced an artifact near the transducers, however, the more important consequence was
942 that during periods of high concentration, the assumption that $r\alpha_s \ll 1$, resulted in a significant
943 overestimate of particle size and underestimate of concentration in the bottom 0.1 m above the
944 bed. The results of introducing uncertainties into the inversion for a_M and M were illustrated in
945 figures 9 and 10. These showed that for no random errors, $\gamma_o=0$, a_M and M provided reasonable
946 estimates for a_c and C for the lower concentration events and not to close to the bed. However,
947 for the higher concentration events and close to the bed, when attenuation was significant, the
948 positive feedback in the implicit iterative formulation led to large errors in the estimated values
949 for a_c and C. Introduction of a random component with $\gamma_o=0.1$, caused further uncertainties
950 which could be significant. To reduce uncertainties in the estimate of M it was shown in figure
951 11 that using a time average profile for a_M in the inversion could improve results for M.

952

953 To more generally assess the impact of uncertainties, a_M/a_c and M/C were evaluated over a wide
954 range of uncertainty levels, for $\varepsilon=0.5$-1.5 with $\gamma_o=0$ and for $\gamma_o=0$-0.2 for $\varepsilon=1$. For the first case
955 $\overline{a_M/a_c} \approx 1$ while $\overline{M/C}$ increasingly diverged from unity. In the second case $\overline{a_M/a_c} \approx 1$, although
956 the standard deviation increased with γ_o while for $\overline{M/C}$ both the mean estimate and standard
957 deviation increased substantially with γ_o. For the case when profiles of $\overline{a_M}$ were used and only

958   high temporal-spatial values of M were being estimated, the mean value for $\overline{M/C}$ remained close

959   to unity as γ_o increased and the region of uncertainty was substantially reduced.

960

961   The value for a_M obtained from the acoustic inversion is not the size most sedimentologists use

962   to categorise the suspension. Sedimentologists use the median mass diameter, d_{50}, and it is d_{50}

963   which is used in most sediment transport formulae. The relationship between a_M and d_{50} depends

964   on the probability density function of m(a), and depending on the distribution estimated for n(a)

965   obtained from fitting m(a) to a measured mass size distribution, the results for the relationship

966   can be problematic. The more prudent approach would be to assume the particles were nominally

967   spherical and convert each size fraction of the measured mass distribution into a number size

968   distribution, formulate n(a), and either fit an analytic distribution to n(a) or use the actual

969   measured distribution. In either case, n(a) will need to be related to m(a) to convert the acoustic

970   measurement of a_M to the usually accepted size of d_{50} used in most sediment transport

971   formulations.

972

973   Finally this article has aimed at providing an overview of the application of acoustics to the

974   measurement of suspended sediment profiles over inorganic non-cohesive beds. The theoretical

975   background, statistics, and errors have been examined through a limited number of scenarios. It

976   is not possible to cover all situations which will be encountered in the field, but this work does

977   aim to provide some guidance as to what may be expected especially when vertical size sorting is

978   present. From the results obtained here, it is suggested that it would be judicious not only to

979   carry out inversions with best estimates of system calibration and suspension scattering

980   characteristics, but to also adjust these values within the bounds of expected uncertainties to

981   ascertain the impact on the acoustic estimates of a_M and M.

982

992   **APPENDIX 1.** The forward problem; calculating the backscattered signal.

993   Here a précis of the acoustic backscattering from an aqueous suspension is outlined. The
994   amplitude of the backscattered signal, V, from a particle in the beam of an ABS using a disc
995   transceiver can be expressed as (Sheng and Hay, 1998; Thorne and Hanes, 2002)

996     $$V = \frac{af_i V_T T_s R_s g_R D^2(\theta)\, e^{-2r\alpha_w}}{2r^2}$$ A1.1

997   a is the particle radius, f_i is the intrinsic backscatter form function (Vogt and Neubauer, 1976),
998   V_T is the transmit voltage, T_s is the transmit sensitivity, R_s is the receive sensitivity, g_R is the
999   voltage gain of the receiver, $D(\theta)$ is the transceiver directivity function, θ is the angle the scatter
1000   subtends to the acoustic axis, r is the range to the particle and α_w is the attenuation due to water
1001   absorption. For incoherent scattering from an elemental volume, δv, with N particles per unit
1002   volume, the elemental mean-square backscattered signal is (Clay and Medwin, 1997)

1003 $$\delta V_m^2 = \{V^2\} N \delta v$$ A1.2

1004   where { } represents an average over a number of independent backscatter signals squared, V^2.
1005   For a circular transceiver the elemental volume can be written as $\delta v = r^2 \sin\theta d\theta d\phi dr$ allowing V_m^2
1006   to be expressed as

1007 $$V_m^2 = f^2 (V_T T_s R_s g_R)^2 \frac{3M}{16\pi\rho<a>} \int_{r-r_o/4}^{r+r_o/4} \int_0^{\pi/2} \int_0^{2\pi} \frac{e^{-4r\alpha}}{r^2} D^4 \sin\theta d\phi d\theta dr$$ A1.3

1008   N has been replaced by the mass concentration, M, ρ is the particle density, r_o is the transmitted
1009   pulse length and $f^2 = <a><a^2 f_i^2/\rho>/<a^3>$, where $< >$ represents an average over the particle size
1010   distribution, n(a). The integrals can be readily evaluated (Hay, 1991; Thorne and Hardcastle,
1011   1997) resulting in

1012 $$V_m^2 = \left(\frac{K\Re}{r\psi}\right)^2 M e^{-4(r\alpha_w + \alpha_s)}$$ A1.4

1013

1014   where

$$\psi = \frac{1 + 1.35\left(\frac{r}{r_n}\right) + (2.5\frac{r}{r_n})^{3.2}}{1.35\left(\frac{r}{r_n}\right) + (2.5\frac{r}{r_n})^{3.2}}$$

1015

$$K = \left(\frac{f^2}{<a>}\right)^{1/2}; \quad \alpha_s = \int\limits_0^r \xi M dr; \quad \xi = \frac{3\chi}{4<a>}; \quad \Re = V_T T_s R_s g_R \left(\frac{3\tau}{16}\right)^{0.5} \frac{0.96}{ka_t}$$

1016

1017 α_s is the sediment attenuation, ψ is a transducer nearfield correction factor (Downing et al 1995),

1018 $r_n = \pi A_t^2/\lambda$ is the transducer nearfield, A_t the transducer radius, $\chi = <a><a^2\chi_i/\rho>/<a^3>$, χ_i is the

1019 intrinsic normalised total backscattering cross-section (Thorne et al, 1993; Schaafsma and Hay,

1020 1997; Moate and Thorne, 2013), k is the wavenumber of the sound in water and a_t is the radius of

1021 the transceiver. Equation (A1.4) represents the forward scattering problem; if the composition of

1022 the suspension is known the backscattered signal can be calculated. It is the backscattered signal

1023 calculated by equation (A1.4), with systematic, ε, and random γ_o errors introduced, using the

1024 suspension field given in figure 4 with the n(a) in figure 3 that is used in the inversion scenarios.

1025 In the present study the focus is on the rearrangement of equation (A1.4) making M the

1026 dependent variable, as presented in equation (1), and estimating M and $a_M = a_o$ (<a>) through

1027 inversion methodologies.

1028

1029

1030   **APPENDIX 2.** Methodology for estimating a_M and M.

1031   Here the procedure for extracting particle size is illustrated. To obtain particle size and

1032   concentration from the acoustic inversion requires a methodology to calculate size. A number of

1033   approaches have been adopted (Hay and Sheng, 1992; Crawford and Hay 1993, Thorne and

1034   Hardcastle, 1997; Thosteson and Hanes, 1998; Thorne et al 2007). These approaches have been

1035   examined and that of Thorne et al 2007 was found to be at least as robust as any of the

1036   approaches and generally better. However, the approach is computationally intensive, with

1037   equations (1-3,6-8) being solved for a range of a_o, at each of the three frequencies, 0.75, 1.25 and

1038   3.0 MHz, and sequentially along the backscattered profile. Equation (8) outlines the procedure

1039   where a solution for a_o is sought by minimizing $\Phi = \sigma_M(a_o)/M(a_o)$, where σ_M is the standard

1040   deviation and M the mean mass, obtained from the three frequencies, for each value of a_o, over a

1041   prescribed range of a_o, sequentially at each range bin.

1042

1043   To illustrate the particle size inversion process, one single backscatter profile from the

1044   suspension field shown in figure 4, has been inverted using equations (1-3, 6-8) with n(a), for

1045 $a_o=2$-400 μm with a step interval of $\delta a_o=2$μm and the result for Φ is shown in figure A2.1a

1046   between 1-200 μm for clarity. For the calculation $\varepsilon=1$, $\gamma=0$, the nearfield correction was applied

1047   and account was taken of sediment attenuation. The figure clearly shows a minimum occurring

1048   in the surface of Φ with z and a_o. The locus of the minima for a_o yields a_M which is plotted in

1049   figure A2.1b with height above the bed, z, and compared with the a_c profile. As can be observed,

1050   within the step interval of δa_o, the value for a_M is in agreement with a_c. In figure A2.1c the

1051   profile of M, associated with the minimum value of Φ is compare with C and good agreement is

1052   observed. The same process has been repeated in figures A2.1d-A2.1f for a suspension field

1053   having twice the particle size and in figures A2.1g-A2.1i for a suspension field having half the

1054   particle size. As can be seen the inversion was successful in all three cases.

1055

1056

1057   **APPENDIX 3.** Using two or three frequency ABS inversion

1058   When a three frequency ABS is deployed three backscattered signal are collected. These can be

1059   used as frequency pairs to obtain three estimates of a_M and M by minimizing Φ for each pair.

1060   Alternatively all three frequencies can be combined and Φ minimised to give a single estimate

1061   for a_M and M. To examine each approach $\bar{a}_c$ and $\bar{C}$ were used and backscatter signals calculated

1062   as systematic and random errors were both varied independently at each frequency over values

1063   between ε=0.975-1.025 and γ_o=0.025 and 100 backscattered realization were computed. A full

1064   inversion was carried out using equations (1-3, 6-8) with the nearfield correction applied and

1065   account taken of sediment attenuation. The 100 profiles of a_M and M were respectively

1066   normalised by $\bar{a}_c$ and $\bar{C}$. The results are shown in figure A3.1, the outcome from the three

1067   frequency pairs is indicated by the light grey data points and from the three frequency

1068   combination by the darker grey points, the solid lines are a_M/a_c and M/C for ε=1, γ_o=0. It can be

1069   clearly seen that the impact of errors on the two frequency inversions is significantly greater than

1070   for the three frequency inversion. The three frequency inversion reduces the degree of ambiguity

1071   in a_M, due to the form of K, and adds stability by further constraining the inversion.

1072

1073

1074

1075 **APPENDIX 4.** Impact of particle size on inversion uncertainties.

1076   To assess the impact of particle size on the accuracy and uncertainty of a_M and M, the inversions

1077 carried out to provide the data for figure 12 were repeated using the same C field but with

1078 particle radii of $1.5a_c$ and $a_c/1.5$. The results are presented in figures A4.1a-A4.1c for $1.5a_c$ and

1079 A4.1d-A4.1f for $a_c/1.5$ using the same nomenclature as figure 12 and they show that when the

1080 particle size increased $\overline{M/C}$ accuracy improved and uncertainties decreased, while when particle

1081 size reduced accuracy decreased and uncertainties increased. The difference with particle size is

1082 due to the dependence of M on a_o; when x<1 the dependency of M on a_o tends to a_o^3, which

1083 increases the variability and bias of $\overline{M/C}$, while increases in a_o lead to a weaker dependency of M

1084 on a_o for x≥1, resulting in reduced uncertainty and bias in $\overline{M/C}$. The result of using $\overline{a_m}$ and re-

1085 computing M yielded more accurate and less variable estimates of M.

1086

1087 **REFERENCES**

1088 Amoudry, L. O., and Souza A.J., 2011. Deterministic coastal morphological and sediment
1089 transport modeling: A review and discussion, Rev. Geophys., 49, RG2002,
1090 doi:10.1029/2010RG000341.

1091

1092 Betteridge, K.F.E., Thorne, P.D. and Cooke, R.D., 2008. Calibrating multi-frequency acoustic
1093 backscatter systems for studying near-bed suspended sediment transport processes. Continental
1094 Shelf Research., 28, 227-235.

1095

1096 Bolanos R, Thorne PD and Wolf J. 2012.Comparison of measurements and models of bed stress,
1097 bedforms and suspended sediments under combined currents and waves. Coastal Engineering 62,
1098 19-30.

1099

1100 Clay C. S. and Medwin H. 1997. Acoustical Oceanography. Published by John Wiley and Sons,
1101 Canada.

1102

1103 Crawford, A.M., Hay, A.E., 1993. Determining suspended sand size and concentration from
1104 multifrequency acoustic backscatter. J. Acoust. Soc. Am. 94(6), 3312-3324.

1105

1106 Davies A. G. and Thorne P.D. 2008. Advances in the study of moving sediments and evolving
1107 seabeds. Surveys in Geophysics Vol 29, No 1, January, 1-36.
1108
1109 Downing, A., Thorne, P.D. and Vincent, C.E., 1995. Backscattering from a suspension in the
1110 near field of a piston transducer. Journal Acoustical Society of America, 97 (3), 1614-1620.

1111

1112 Faran J.J. 1951. Sound scattering by solid cylinders and spheres. Journal Acoustical Society of
1113 America. Vol. 23 (4) 405-418.

1114

1115 Gaunaurd G. C. and Uberall H. 1983. RST analysis of monostatic and bistatic acoustic echoes
1116 from an elastic sphere. Journal Acoustic Society of America Vol. 73 (1) 1-12.

1117

1118 Gordon, L, 1996, Acoustic Doppler current profiler—Principles of operation: A practical primer:
1119 RD Instruments, San Diego, CA, pp41 available at http://www.comm-
1120 tec.com/Library/Technical_Papers/RDI/Broadband%20Primer.pdf.

1121

1122 Hay A. E., 1983. On the remote acoustic detection of suspended sediments at long wavelengths.
1123 Journal of Geophysical Research, 88, C12, 7525-7542.

1124

1125 Hay, A.E., 1991. Sound scattering from a particle-laden turbulent jet, J. Acoust. Soc. Am., 90,
1126 2055-2074.

1127

1128 Hay, A.E., Sheng. J., 1992. Vertical profiles of suspended sand concentration and size from
1129 multifrequency acoustic backscatter. J. Geophys. Res. 97(C10). 15661-15677.

1130

1131 Hay, A.E., and Bowen, A.J., 1994. Coherence scales of wave-induced suspended sand
1132 concentration fluctuations. Journal of Geophysical Research 99 (C6), 12749–12765.
1133 doi:10.1029/94JC00290.

1134

1135 Hay A. E., 2011. Geometric bottom roughness and the bed state storm cycle. Journal of
1136 Geophysical Research, 116. C04017, doi:1029/2010JC006687.

1137

1138 Hay A.E., Zedel L., Cheel R. And Dillon J., 2012. On the vertical and temporal structure of flow
1139 and stress within the turbulent oscillatory boundary layer above evolving beds. Continental Shelf
1140 Research, 46, 31-49.

1141

1142 Heathershaw A. D. 1976. Measurements of turbulence in the Irish Sea benthic boundary layer.
1143 The Benthic Boundary Layer edited by I.N. McCave and published by Plenum publishing
1144 Corporation New York USA, 11-31. ISBN: 978-1-4615-8749-1

1145

1146 Holdaway, G.P. Thorne, P.D., Flatt, D., Jones, S.E., Prandle, D. 1999. Comparison between
1147 ADCP and transmissometer measurements of suspended sediment concentration. Continental
1148 Shelf Research 19 421-441.

1149

1150 Hurther D., Lemmin U., Terray E. A., 2007. Turbulent transport in the outer region of rough wall

1151 open-channel flows: the contribution of Large Coherent Shear Stress Structures (LC3S). Journal

1152 of Fluid Mechanics 574, 465-493.

1153

1154 Hurther D. and Thorne P.D. 2011. Suspension and near-bed load sediment transport processes

1155 above a migrating, sand-rippled bed under shoaling waves. J. Geophys. Res., Vol 116, C07001,

1156 doi:1029/2010JC006774.

1157

1158 Hurther, D, Thorne, PD and Bricault M, Lemmin U and Baroud JM. 2011. A multi-frequency

1159 acoustic concentration and velocity profiler (ACVP) for boundary layer measurements of fine-

1160 scale flow and sediment transport processes. Coastal Engineering. 58, 294-605   doi:

1161 10.1016/j.coastaleng.2011.01.006.

1162

1163 Libicki, C., Bedford, K.W., Lynch, J.F., 1989. The interpretation and evaluation of a 3-MHz

1164 acoustic backscatter device for measuring benthic boundary layer sediment dynamics, J. Acoust.

1165 Soc. Am. 1501-1511.

1166

1167 Moate B. D. and Thorne P. D., 2009. Measurements and inversion of acoustic scattering from

1168 suspensions having broad size distributions. Journal Acoustical Society America, 126(6), 2905-

1169 1917.

1170

1171 Moate B.D. and Thorne P.D. 2012. Interpreting acoustic backscatter from suspended sediments

1172 of different and mixed mineralogical composition. Continental Shelf Research, 46, 67-82.

1173

1174 Moate B.D. and Thorne P.D., 2013. Scattering from suspended sediments having different and

1175 mixed mineralogical compositions: Comparision of laboratory measurements and theoretical

1176 predictions. Journal Acoustical Society America 133(3) 1320-1334.

1177

1178   Moore, S. A., Le Coz J., Hurther D. and Paquier A. 2012. On the application of horizontal
1179   ADCPs to suspended sediment transport surveys in rivers. Continental Shelf Research, 46, 50-
1180   63.

1181

1182   Moore, S. A., Le Coz J., Hurther D. and Paquier A. 2013. Using multi-frequency acoustic
1183   attenuation to monitor grain size and concentration of suspended sediment in rivers. Journal
1184   Acoustical Society America, 133(4), 1959-1970.

1185

1186   Morse P. M. and Ingard K. U. 1987. Theoretical Acoustics. Princeton University Press. Chap 8.
1187   pp949.

1188

1189   O'Hara Murray, Hodgson D.M. and Thorne P.D., 2012. Wave groups and the character of
1190   sediment resuspension over an evolving sandy bedforms. Continental Shelf Research, 46, 16-30.

1191

1192   Pedocchi F, and Garcia M. H. 2012. Acoustic measurement of suspended sediment concentration
1193   profiles in an oscillatory boundary layer. Continental Shelf Research, 46, 87-95.

1194

1195   Richards S.D., Leighton T.G. and Brown N.R., 2003. Visco-inertial absorption in dilute
1196   suspensions of irregular particles. Proceedings of the Royal Society London, 459, 2153-2167.

1197

1198   Schaafsma A. S. and Hay A. E. 1997. Attenuation in suspensions of irregularly shaped sediment
1199   particles: A two-parameter equivalent spherical scatterer model. Journal Acoustical. Society of
1200   America. 102, 1485-1502.

1201

1202   Sheng, J. and Hay, A.E., 1988. An examination of the spherical scatterer approximation in
1203   aqueous suspensions of sand, J. Acoust. Soc. Am., **83**: 598–610.

1204

1205   Simmons S.M., Parsons D.R., Best J.L., Orfeo O., Lane S.N., Kostaschuk R., Hardy R.C., West
1206   G., Malzone C., Marcus J. and Pocwiardowski P., 2010. Monitoring Suspended Sediment
1207   Dynamics Using MBES. Journal of Hydraulic Engineering, January, 45-49.

1208

1209 Smerdon, A.M. & Caine, S.J., 2007, "A commercial multi-frequency acoustic backscatter
1210 instrument for profiling of suspended sediment size distribution and load", Hydraulic
1211 Measurements & Experimental Methods Conference. Book of Extended Abstracts of the
1212 Specialty Conference. September 10-12, 2007, Lake Placid, NY, Environmental & Water
1213 Resources Institute of the American Society of Civil Engineers and the International Association
1214 of Hydraulic Engineers.

1215

1216 Soulsby, R.L., 1997. Dynamics of Marine Sands. A Manual for Practical Applications. Thomas
1217 Telford publications, London, UK.

1218 Thorne, P.D., Hardcastle, P.J., and Soulsby, R.L., 1993. Analysis of acoustic measurements of
1219 suspended sediments. Journal of Geophysical Research, 98 (C1), 899-910.

1220 Thorne, P.D., Hardcastle, P.J., Flatt, D. and Humphery, J.D. 1994. On the use of acoustics for
1221 measuring shallow water suspended sediment processes. IEEE Journal of Oceanic Engineering,
1222 19(1), 48-57.

1223

1224 Thorne, P.D., Holdaway, G.P and Hardcastle, P.J. 1995. Constraining acoustic backscatter
1225 estimates of suspended sediment concentration profiles using the bed echo. J.Acoust. Soc. Am.
1226 98(4), 2280-2288.

1227

1228 Thorne, P.D. and Hardcastle, P.J., 1997. Acoustic measurements of suspended sediments in
1229 turbulent currents and comparison with in-situ samples. Journal of the Acoustical Society of
1230 America 101 (5) (Pt. 1), 2603-2614.

1231

1232 Thorne, P.D. and Hanes, D.M., 2002. A review of acoustic measurement of small-scale sediment
1233 processes. Cont. Shelf Res., 22, 603-632.

1234

1235 Thorne, P.D., Agrawal, Y.C. and Cacchione, D.A., 2007. A Comparison of Near-Bed Acoustic
1236 Backscatter and Laser Diffraction Measurements of Suspended Sediments. IEEE Journal of
1237 Ocean Engineering., 32 (1), 225-235.

1238

1239 Thorne, P.D. and Meral, R., 2008. Formulations for the scattering properties of sandy sediments
1240 for use in the application of acoustics to sediment transport. Journal of Continental Research, 28,
1241 309-317.

1242
1243
1244 Thorne P. D., Davies A. G. and Bolanos R., 2011a. Measurement and modelling of suspended
1245 sediment size profiles above sandy rippled beds under waves. Published in the proceedings of
1246 Coastal Sediments 2011, held in Miami, Florida, USA, 2 May – 6 May 2011, edited by Julie D
    Rosati, Ping Wang and Tiffany M Roberts. ISBN: 978-981-4355-52-0. 1620-1633.

1247
1248 Thorne P. D., Hurther D. and Moate B. D. 2011b. Acoustic inversions for measuring boundary
1249 layer suspended sediment processes. J Acoust Soc Amer 130(3) 1188-1200.
1250 DOI:10.1121/1.3618728.

1251
1252 Thorne P. D. and Hay A.E. 2012. Introduction to the special issue of Continental Shelf Research;
1253 On the application of acoustics to sediment transport processes. Continental Shelf Research, 46,
1254 1.

1255
1256 Thosteson, E.D. and Hanes, D.M., 1998. A Simplified method for determining sediment size and
1257 concentration from multiple frequency acoustic backscatter measurements. Journal Acoustic
1258 Society of America 104(2), Pt.1, 820-830.

1259
1260 Traykovski P., 2007. Observations of wave orbital scale ripples and a nonquilibrium time-
1261 dependent model. Journal of Geophysical Research, 112, C06026, 19pp,
1262 doi:10.1029/2006JC003811

1263
1264 van der Werf, J. J., Magar, V. Malarkey, J. Guizien, K and O'Donoghue. T., 2008. 2DV
1265 modelling of sediment transport processes over full-scale ripples in regular asymmetric
1266 oscillatory flow. Continental Shelf Research, 28, 1040–1056.

1267
1268 Villard, P.V., Osborne, P.D., Vincent, C.E., 2000. Influence of wave groups on SSC patterns
1269 over vortex ripples. Continental Shelf Research 20 (17), 2391–2410.

1270

1271   Vincent, C.E., Hanes, D.M., Bowen, A.J., 1991. Acoustic measurements of suspended sand on

1272   the shoreface and the control of concentration by bed roughness, Marine Geology, 96, 1-18.

1273

1274   Vincent, C.E., Marsh, S.W., Webb, M.P., and Osborne P. D.1999.   Spatial and temporal

1275   structures of suspension and transport over megaripples on the shore face, Journal of

1276   Geophysical Research, Vol. 104(C5), 11,215-11,224.

1277

1278   Vogt R. H. and Neubauer W G. 1976 Relationship between acoustic reflection and vibrational

1279   modes of elastic spheres. Journal Acoustic Society of America, Vol. 60 (1) 15-22.

1280

1281   Wilhelmij P and Denbigh P., 1984. A statistical approach to determining the number density of

1282   random scatterers from backscattered pulses. Journal Acoustical Society America, 76(6) 1810-

1283   1818.

1284

1285

1286 **FIGURE CAPTIONS**

1287 Figure 1. a) Probability density function of the particle size number, n(a), for normal, lognormal

1288 and bi-normal distributions. b) and c) Impact on the backscattering, K, and attenuation, ξ,

1289 scattering characteristics due to a size distribution. The solid line represents intrinsic values and

1290 the symbols ensemble values integrated over the three distributions for n(a) shown in a).

1291

1292 Figure 2. Measurement of the backscattered statistics. a) Normalised backscattered squared

1293 voltage probability density function, b) normalised standard error and c) autocorrelation function

1294 of the backscattered signal amplitude. In the legend in a) the numbers refer to frequency in

1295 megahertz and the letters to scatterer type, s-sand, b-bubbles, and the nomenclature applies to the

1296 three plots.

1297

1298 Figure 3. The probability density function for the bed mass size, $m_b(a)$ (---), and the number size,

1299 $n_b(a)$ (—), used for the acoustic inversions. a_{bm} (173 μm) is the mean mass radius, a_{b50} (160 μm)

1300 is the median mass radius and a_{bc} (110 μm) is the mean number radius.

1301

1302 Figure 4. The suspension field used to generate the backscattered signal. a) Time series of a_c with

1303 height above the bed, b) temporally averaged a_c profile, $\bar{a}_c$, and c) temporal variation of a_r at z_r.

1304 d) Time series of C with height above the bed, e) temporally averaged C profile, $\bar{C}$, and f)

1305 temporal variation of C_r at z_r.

1306

1307 Figure 5. 2.0 MHz single frequency inversion for M using $a_o=d_{b50}/2$ and the intrinsic scattering

1308 characteristics, case SF1 in Table 1. a) Temporal structure of M with height above the bed for

1309 $\varepsilon=1$ and $\gamma_o=0$. b) and c) Temporal variation of C (—) and M($\bullet$) respectively at z_r and $z=0.9$ m,

1310 with the grey shaded area representing the uncertainty in M for $\varepsilon=0.8$, 1.2 and $\gamma_o=0.1$. d) $\bar{C}$ (—)

1311 and $\bar{M}$ ($\bullet$) with the shaded area representing the uncertainty in $\bar{M}$ and the dashed line with

1312 account taken of the sediment attenuation and the nearfield in the calculation for $\bar{M}$.

1313

1314 Figure 6. 2.0 MHz single frequency inversion for M using $a_o=a_{bc}$ and ensemble scattering

1315 characteristics, case SF2 in Table 1. a) Temporal structure of M with height above the bed for

1316 $\varepsilon=1$ and $\gamma_o=0$. b) and c) Temporal variation of C (—) and M (●) respectively at z_r and $z=0.9$ m,

1317 with the grey shaded area representing the uncertainty in M for $\varepsilon=0.8$, 1.2 and $\gamma_o=0.1$. d) $\bar{C}$ (—)

1318 and $\bar{M}$ (●) with the shaded area representing the uncertainty in $\bar{M}$ and the dashed line with

1319 account taken of the sediment attenuation and the nearfield in the calculation for $\bar{M}$.

1320

1321 Figure 7. 2.0 MHz single frequency inversion for M using the profile in equation (12b), with

1322 $a_o=a_{bc}(z/z_r)^{-1}$ and the ensemble scattering characteristics, case SF3 in Table 1. a) Temporal

1323 structure of M with height above the bed for $\varepsilon=1$ and $\gamma_o=0$. b) and c) Temporal variation of C (—)

1324 and M (●) respectively at z_r and $z=0.9$ m, with the grey shaded area representing the uncertainty

1325 in M for $\varepsilon=0.8$, 1.2 and $\gamma_o=0.1$. d) $\bar{C}$ (—) and $\bar{M}$ (●) with the shaded area representing the

1326 uncertainty in $\bar{M}$ and the dashed line with account taken of the sediment attenuation and the

1327 nearfield in the calculation for $\bar{M}$.

1328

1329 Figure 8. Multi-frequency inversion for a_M and M with the transducer nearfield correction

1330 ignored, $\psi=1$, sediment attenuation neglected, $r\alpha_s \ll 1$ and no uncertainties $\varepsilon=1$, $\gamma_o=0$, case MF1 in

1331 Table 2. Figures a) and b) respectively show $\overline{a_c}$ (—) and $\overline{a_M}$ (●) and $\bar{C}$ (—) and $\bar{M}$ (●). c) and d)

1332 respectively show the temporal structure of a_M and M with height above the bed. e and f

1333 respectively show the time series for a_r and a_M and C_r and M at z_r.

1334

1335 Figure 9. Results for a_M from a multi-frequency inversion for M and a_M with scattering and

1336 calibration errors introduced, case MF2 in Table 2. a) Temporal mean profiles; $\overline{a_c}$ (—), $\overline{a_M}$ (●)

1337 calculated with $\varepsilon=1$ and $\gamma=0$, and the shaded areas are the bounded regions calculated with $\varepsilon=0.8$,

1338 1.2, and $\gamma_o=0$ (red shaded) and $\varepsilon=0.8$, 1.2 with $\gamma_o=0.1$ (blue shaded). b) and c) are respectively a_M

1339 calculated with $\varepsilon=1.2$, $\gamma_o=0.1$ and $\varepsilon=0.8$, $\gamma_o=0.1$. d) and e) are time series at z_r and $z=0.9$ m above

1340 the bed using the same nomenclature as a).

1341

1342 Figure 10. Results for M from a multi-frequency inversion for M and a_M with scattering and

1343 calibration errors introduced, case MF2 in Table 2. a) Temporal mean profiles; $\bar{C}$ (—), $\bar{M}$ (●)

1344 calculated with $\varepsilon=1$ and $\gamma=0$, and the shaded areas are the bounded regions calculated with $\varepsilon=0.8$,

1345 1.2 and $\gamma_o=0$ (red shaded) and $\varepsilon=0.8$, 1.2 and $\gamma_o=0.1$ (blue shaded). b) and c) are respectively M

1346   calculated with ε=1.2, γₒ=0.1 and ε=0.8, γₒ=0.1. d) and e) are time series at z_r and z=0.9 m above

1347   the bed using the same nomenclature as a).

1348

1349   Figure 11. Results for M re-calculated using $\overline{a_M}$ profile from MF2, case MF3 in Table 2. a)

1350   Temporal mean profiles; $\overline{C}$ (—), $\overline{M}$ (●) calculated with ε=1 and γₒ=0, and the grey shaded area is

1351   the bounded region calculated with ε=0.8, 1.2 and γₒ=0.1. b) and c) are respectively M calculated

1352   with ε=1.2, γₒ=0.1and ε=0.8 γₒ=0.1. d) and e) are the time series at z_r and z=0.9 m above the bed

1353   using the same nomenclature as a).

1354

1355   Figure 12. a) Calculation for the temporal-spatial averages for $\overline{a_M/a_c}$ (x) and $\overline{M/C}$ (+) with error

1356   bars for variations in ε. b) and c) respectively show the variation in $\overline{a_M/a_c}$ (●) and $\overline{M/C}$ (●) with

1357   error bars for increasing γₒ. Also shown in c) is the result for $\overline{M/C}$ (o) using the $\overline{a_M}$ profile for

1358   the calculation of M.

1359

1360   Figure 13. Evaluation of the ratio of the median mass diameter to the acoustic mean diameter,

1361 d_{50}/d_M, with the mass size normalised standard deviation, $\delta=\sigma_m/a_m$, assuming n(a) α m(a)/a³,

1362   (o,x), and from a full acoustic inversion, (●,▲), using profiles $\overline{C}$ and $\overline{a_c}$ for lognormal and

1363   normal probability density functions for m(a). The solid line represents a fit to the lognormal

1364   distribution data.

1365

1366   Figure A2.1. a) The form for ϕ with z and a_o for a single inverted profile backscattered from the

1367   suspension field in figure 4, b) the profile of a_M compared with a_c and c) the profile of M

1368   compared with C. d)-f) repeat calculation with $2a_c$ and g)-i) with $a_c/2$.

1369

1370   Figure A3.1. Using $\overline{a_c}$ and $\overline{C}$ profiles, a) $a_M/\overline{a_c}$ and b) $M/\overline{C}$, were calculated using dual frequency

1371   pair inversions, light grey profiles, and triple frequency inversions, dark grey profiles, for 100

1372   backscattered realization of $\overline{a_M}$ and $\overline{M}$ for values of ε between 0.975-1.025 and γₒ=0.025.

1373

1374   Figure A4.1. Calculations for $\overline{a_M/a_c}$ and $\overline{M/C}$ for suspension fields having particle sizes of $1.5a_c$,

1375   a)-c) and $a_c/1.5$ d)-f). a) and d) variation in $\overline{a_M/a_c}$ (x) and $\overline{M/C}$ (+) with ε, b) and e) and c) and f)

1376   respectively show the variation in $\overline{a_M/a_c}$ ($\bullet$) and $\overline{M/C}$ ($\bullet$) with γ_o. Also shown in c) and f) is the

1377   result for $\overline{M/C}$ (o) using $\overline{a_M}$ profiles for the calculation of M.

1378

1379

1380

1381 **TABLE CAPTIONS**

1382 Table 1. Scenarios used in the single frequency inversion scenarios. Explanations for the
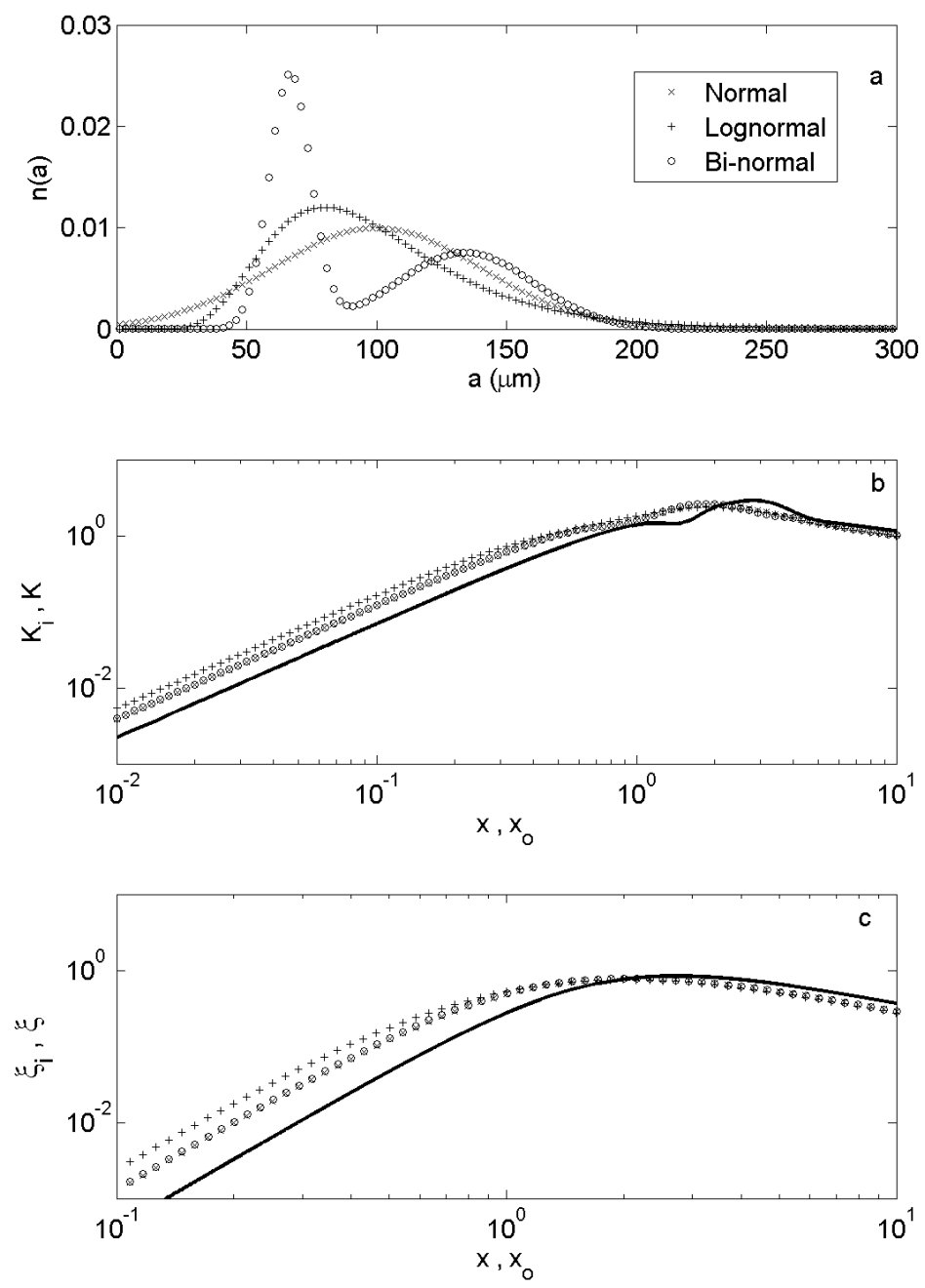
1383 parameters are given in the text.

1384

1385 Table 2. Scenarios used in the multi-frequency inversion scenarios. Explanations for the

1386 parameters are given in the text.

1387

1388

1392   Fig 1. n:\mat5work\sizescatter\ben-mineral\av_chi_fm_scat1.m   8/9/11

1394
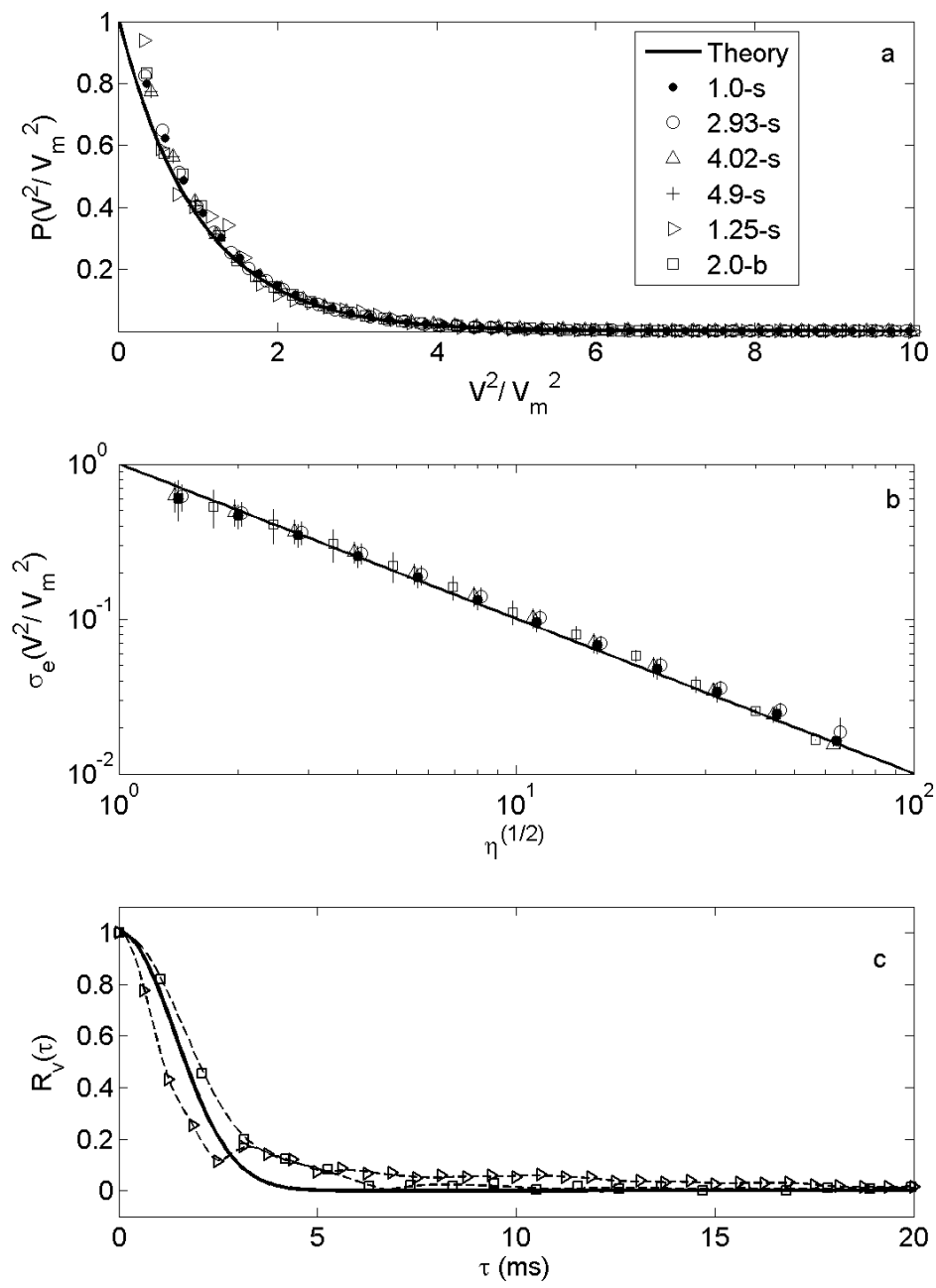
1395
1396   Fig 2.   % n:\mat5work\sizescatter\abs_inversion\plotstats1.m
1397

1398

1399
1400
1401
1402
1403
1404

Fig 3 n:\mat5work\sizescatter\ben-mineral\msize_nsize.m   29/9/11
(distribution of the bed sediments used in text a_n=110, d_{50}=320.
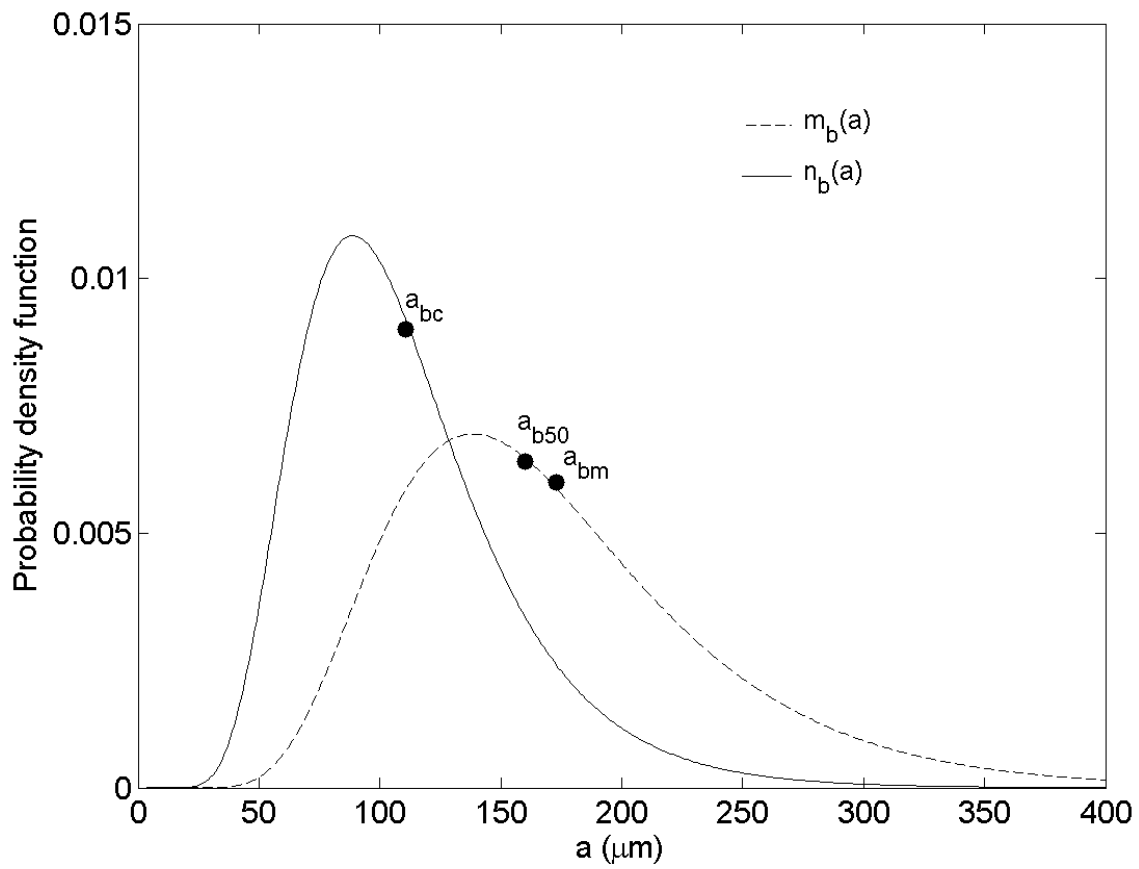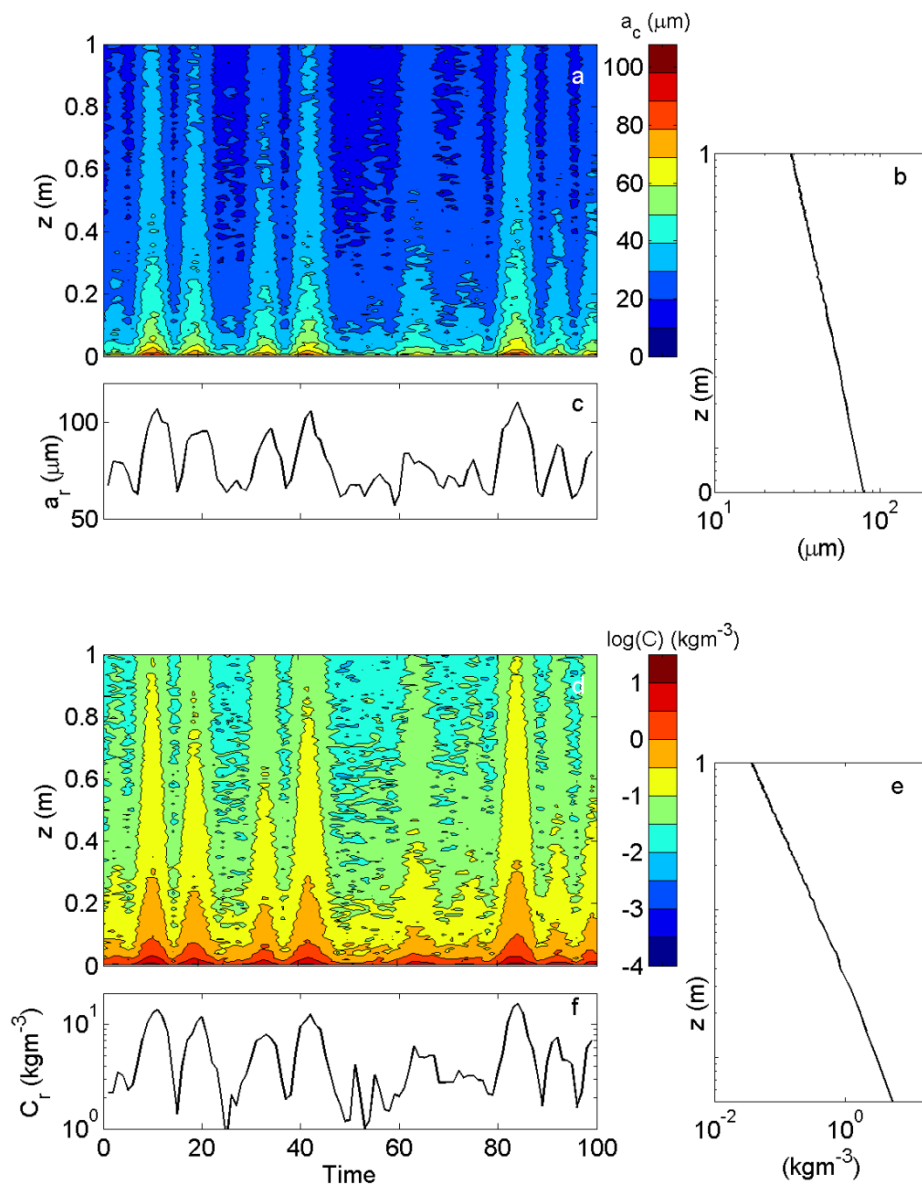
1405
1406
1407
1408
1409
1410
1411
1412

1418
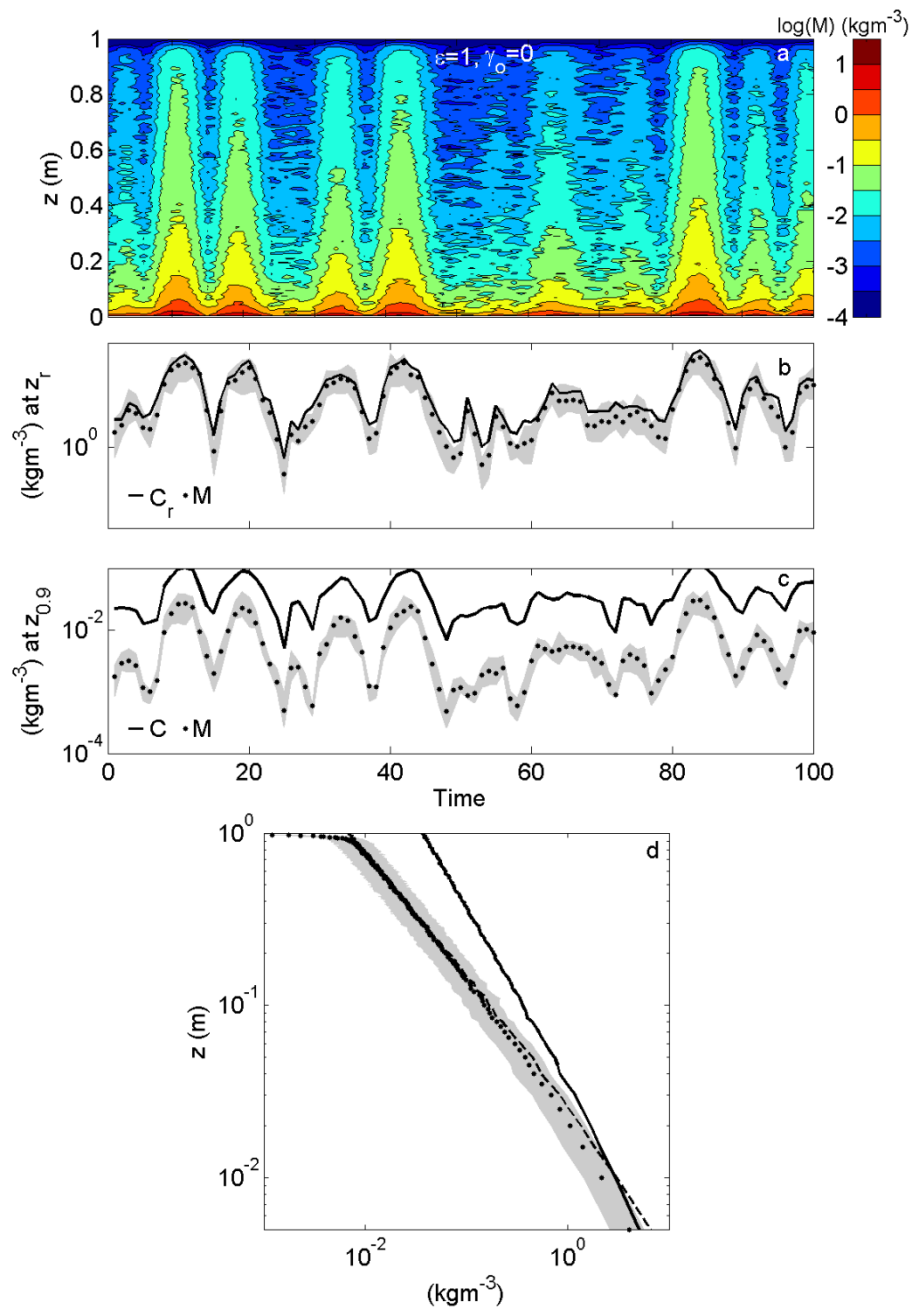
1419

1420   a=d_{50}/2, α_s=0, ψ=1, f_i, χ_i p50 notes 12b
1421   Fig 5. n:\mat5work\sizescatter\abs_inversion\plotc1c.mo/p
1422   n:\mat5work\sizescatter\abs_inversion\press_inv_c1.m i/p
1423   n:\mat5work\sizescatter\abs_inversion\sus_c_a1.m- acfield1c
1424
1425
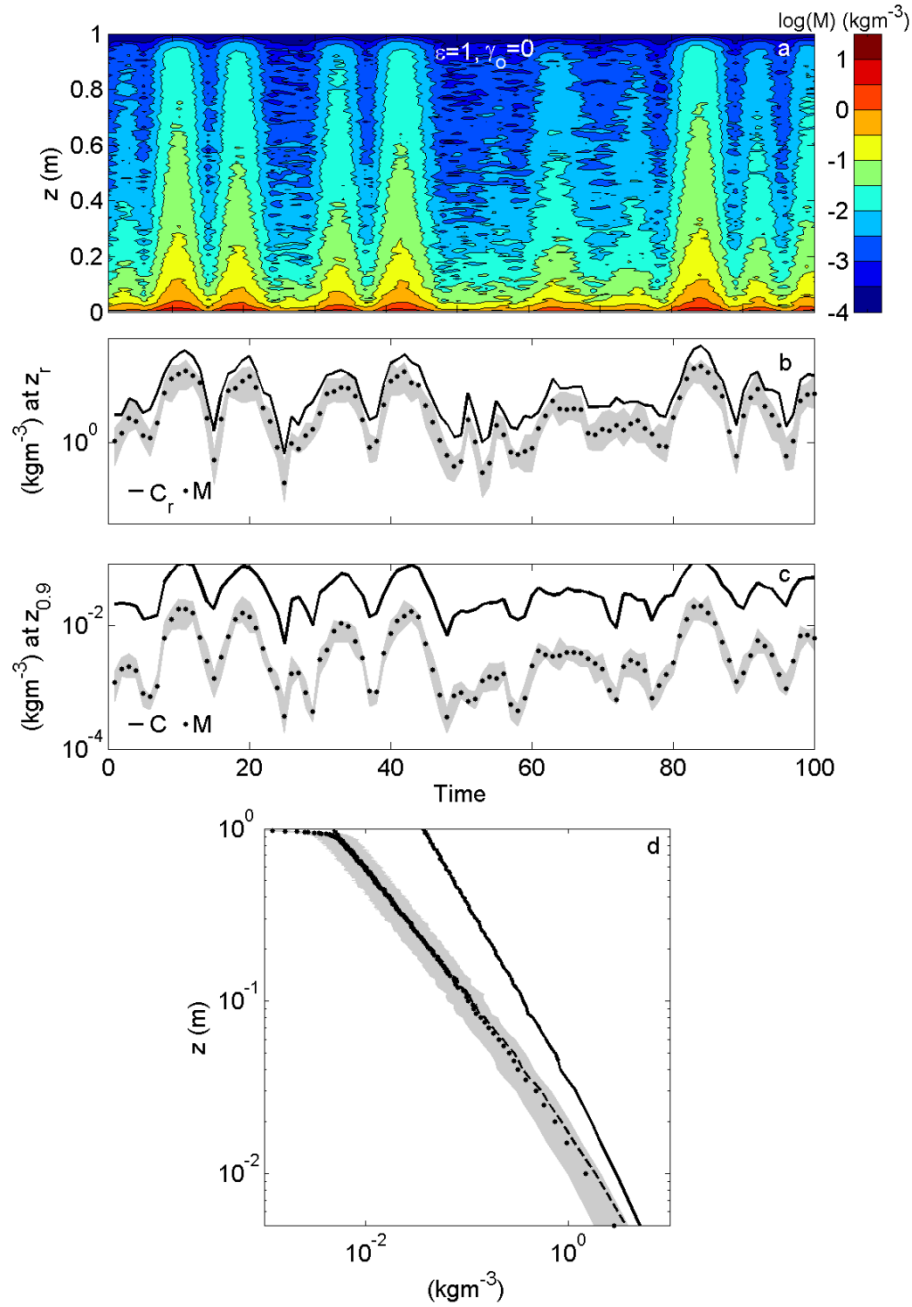
1426
1427
1428   a=a_n of bed α_s=0, ψ=1, f, χ, p48 notes 12b
1429   Fig 6 n:\mat5work\sizescatter\abs_inversion\plotc1c.m
1430   o/p n:\mat5work\sizescatter\abs_inversion\press_inv_c1.m
1431   i/p n:\mat5work\sizescatter\abs_inversion\sus_c_a1.m- acfiled1c
1432
1433

1434
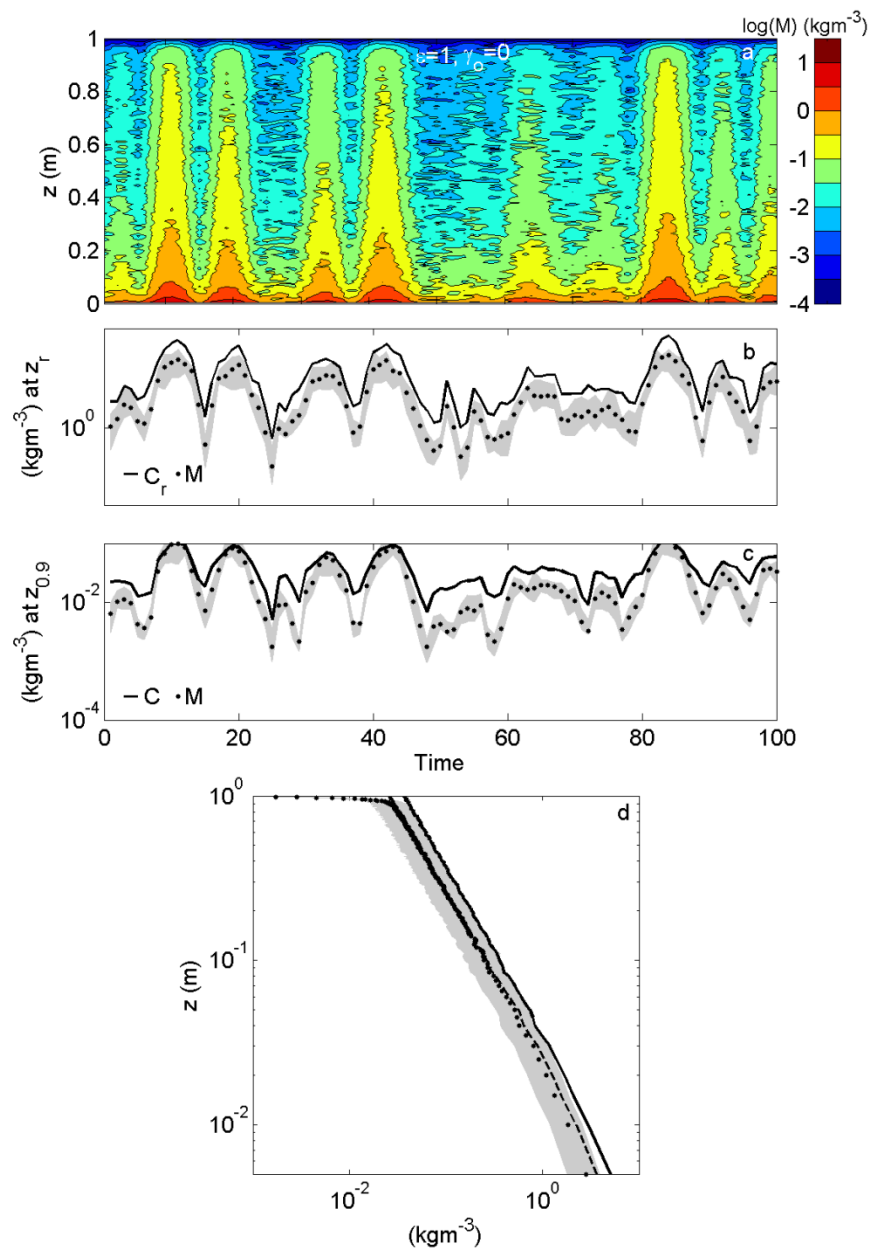
1435
1436   a=an*profile α_s=0, ψ=1, f, χ, p49 notes 12b
1437   Fig 7. n:\mat5work\sizescatter\abs_inversion\plotc1c.m
1438   o/p n:\mat5work\sizescatter\abs_inversion\press_inv_c1.m
1439   i/p n:\mat5work\sizescatter\abs_inversion\sus_c_a1.m- acfiled1c
1440
1441

1442
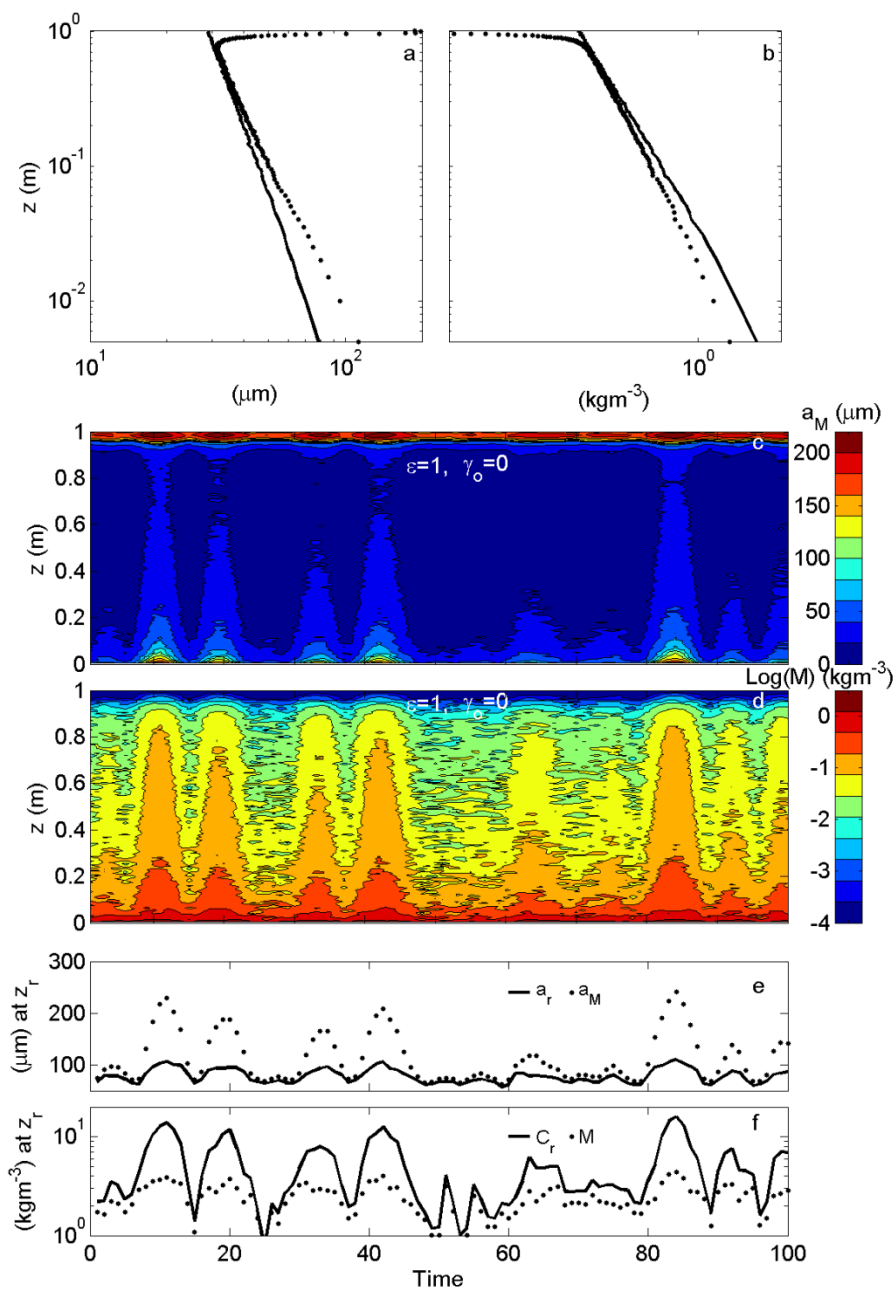
1443
1444
1445   Fig 8. n:\mat5work\sizescatter\abs_inversion\plot_a_c2b.m
1446   o/p n:\mat5work\sizescatter\abs_inversion\inv_press_inv_c_a2.m -   a_M_10ao
1447
1448
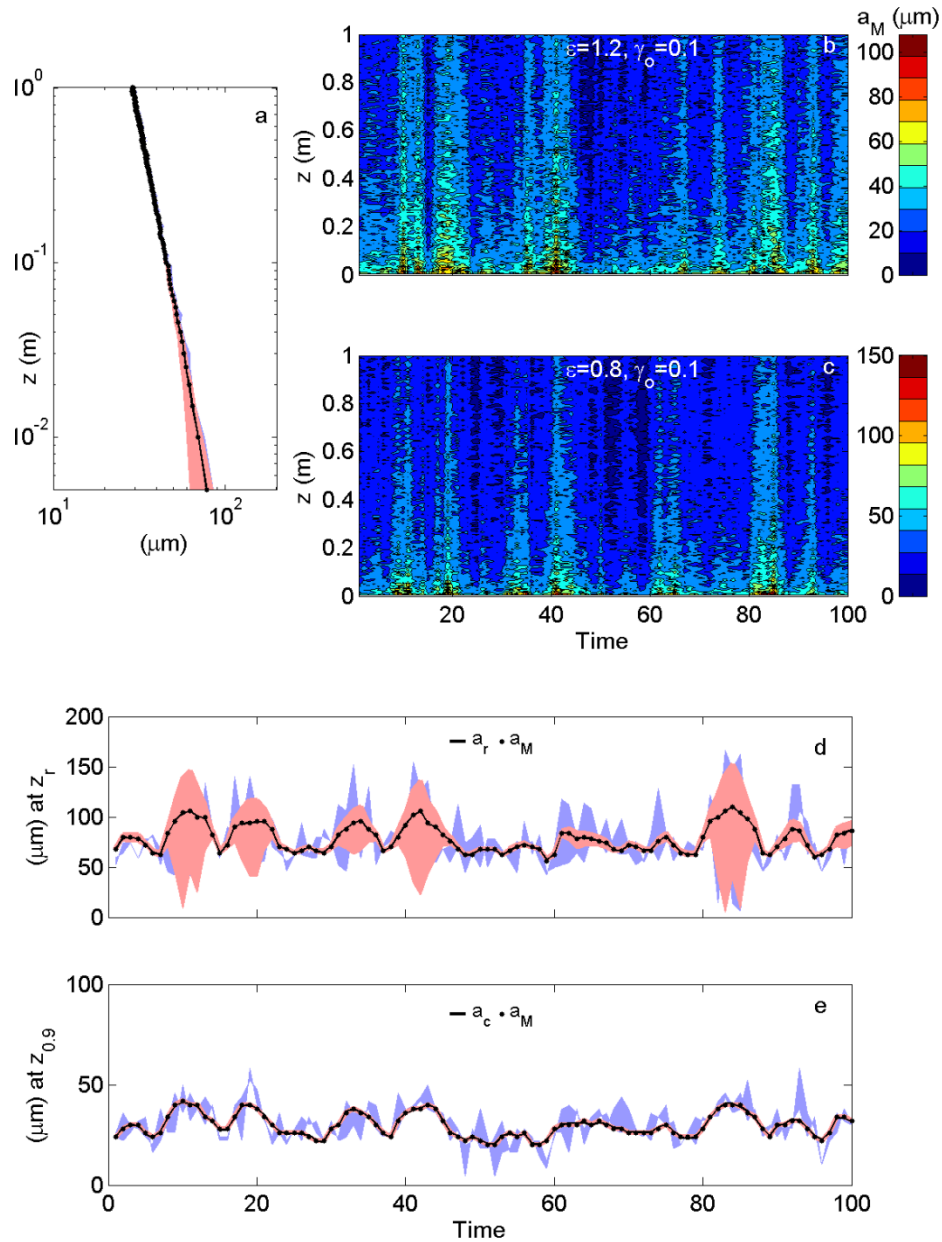
Fig 9. n:\mat5work\sizescatter\abs_inversion\plot_a_c2c_b.m
load acfield1, a_M_00_10, a_M_00_08, a_M_10_08, a_M_00_12, a_M_10_12
i/p from o/p of n:\mat5work\sizescatter\abs_inversion\inv_press_c_2a.m which uses o/p from
press1b.m
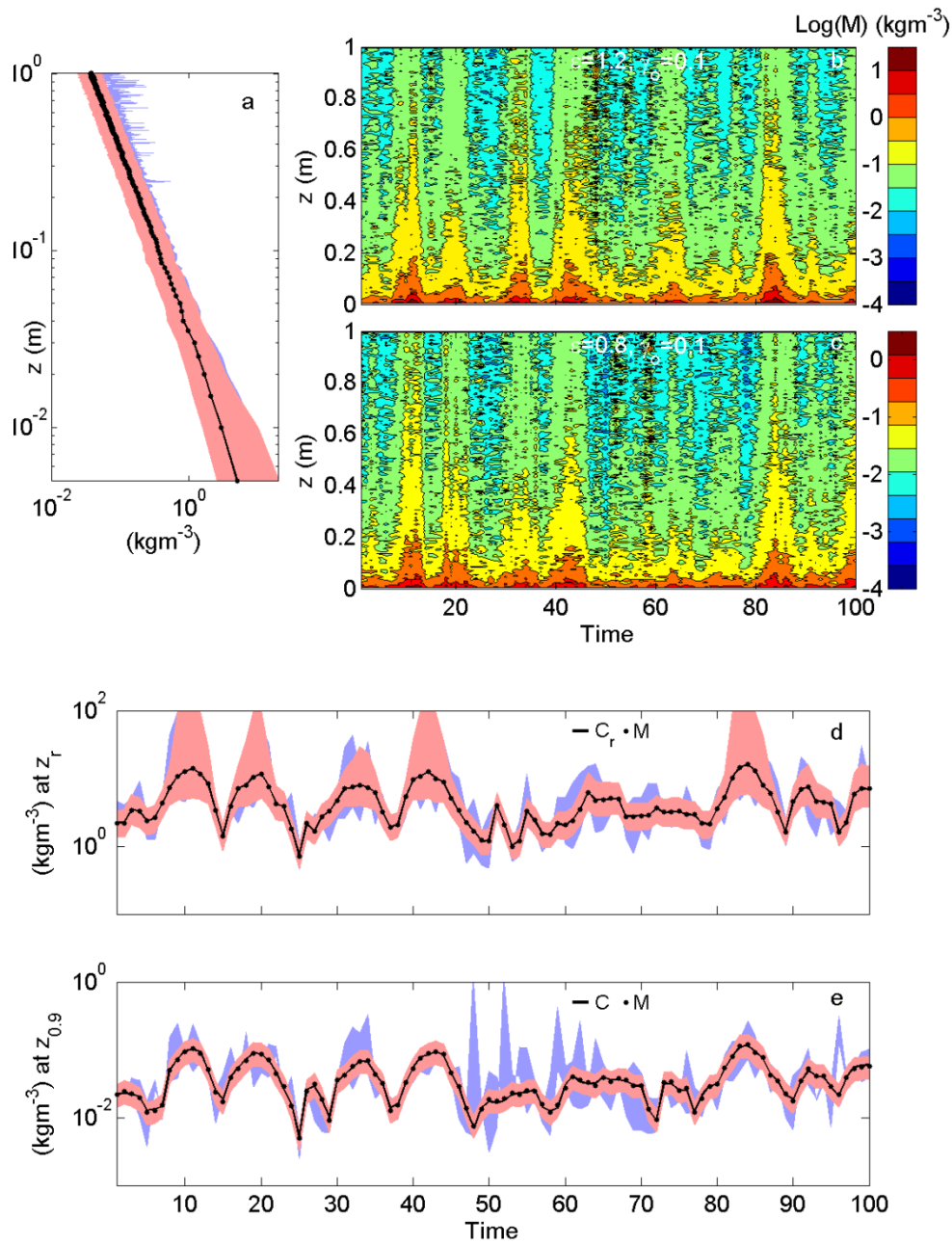
Fig 10. n:\mat5work\sizescatter\abs_inversion\plot_a_c2c_b.m
load acfield1, a_M_00_10, a_M_00_08, a_M_10_08, a_M_00_12, a_M_10_12
i/p from o/p of n:\mat5work\sizescatter\abs_inversion\inv_press_c_2a.m which uses o/p from
press1b.m

1465
1466
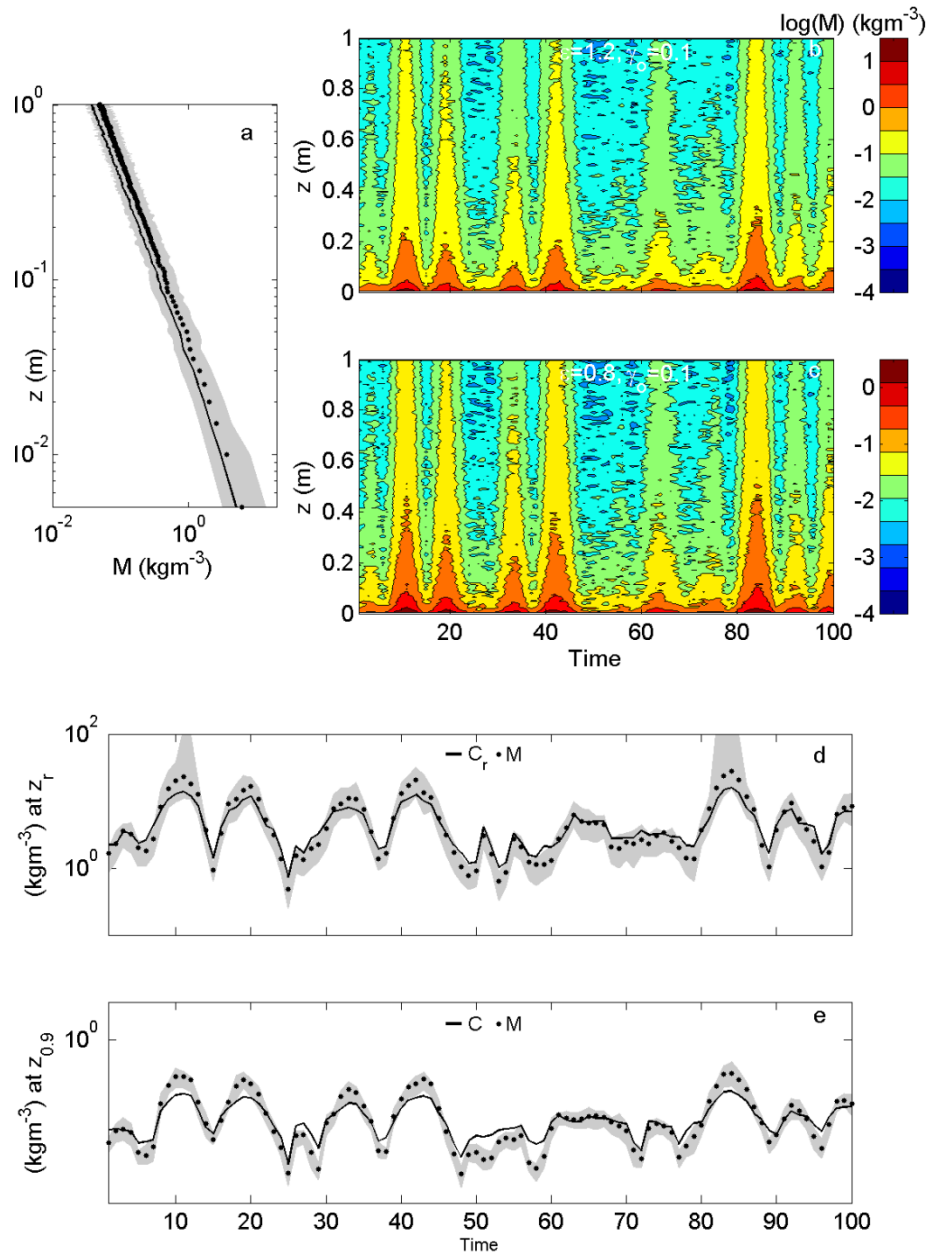
1467
1468   Fig 11. n:\mat5work\sizescatter\abs_inversion\plotc1d.m
1469   o/p n:\mat5work\sizescatter\abs_inversion\press_inv_c2.m
1470   uses mean particle size from triple freq o/p of inv_press_c_a2.m & files from press1b.m to calc
1471   M
1472
1473
1474
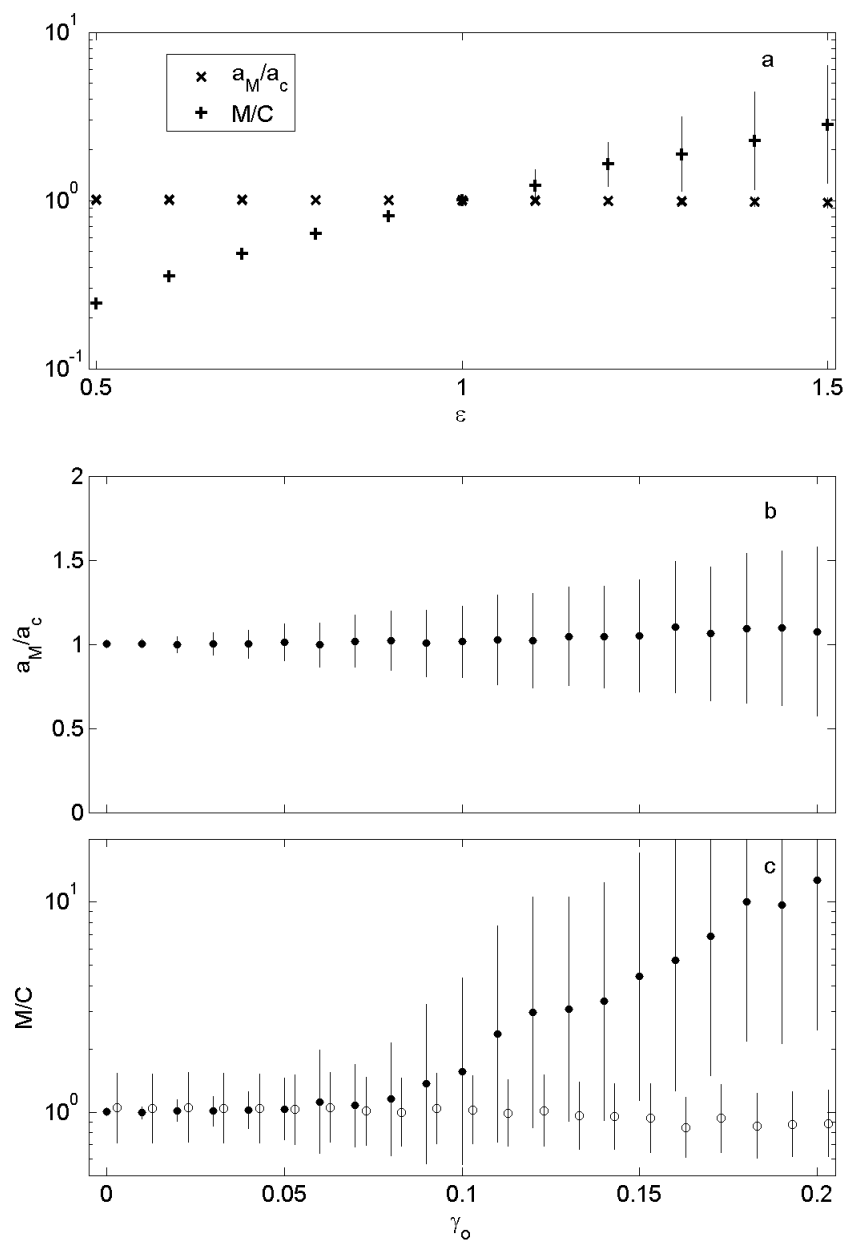
$a = a_c$

Fig 12 n:\mat5work\sizescatter\abs_inversion\plot_err_stats3b.m
takes o/p from % n:\mat5work\sizescatter\abs_inversion\inv_press_c_a3.m
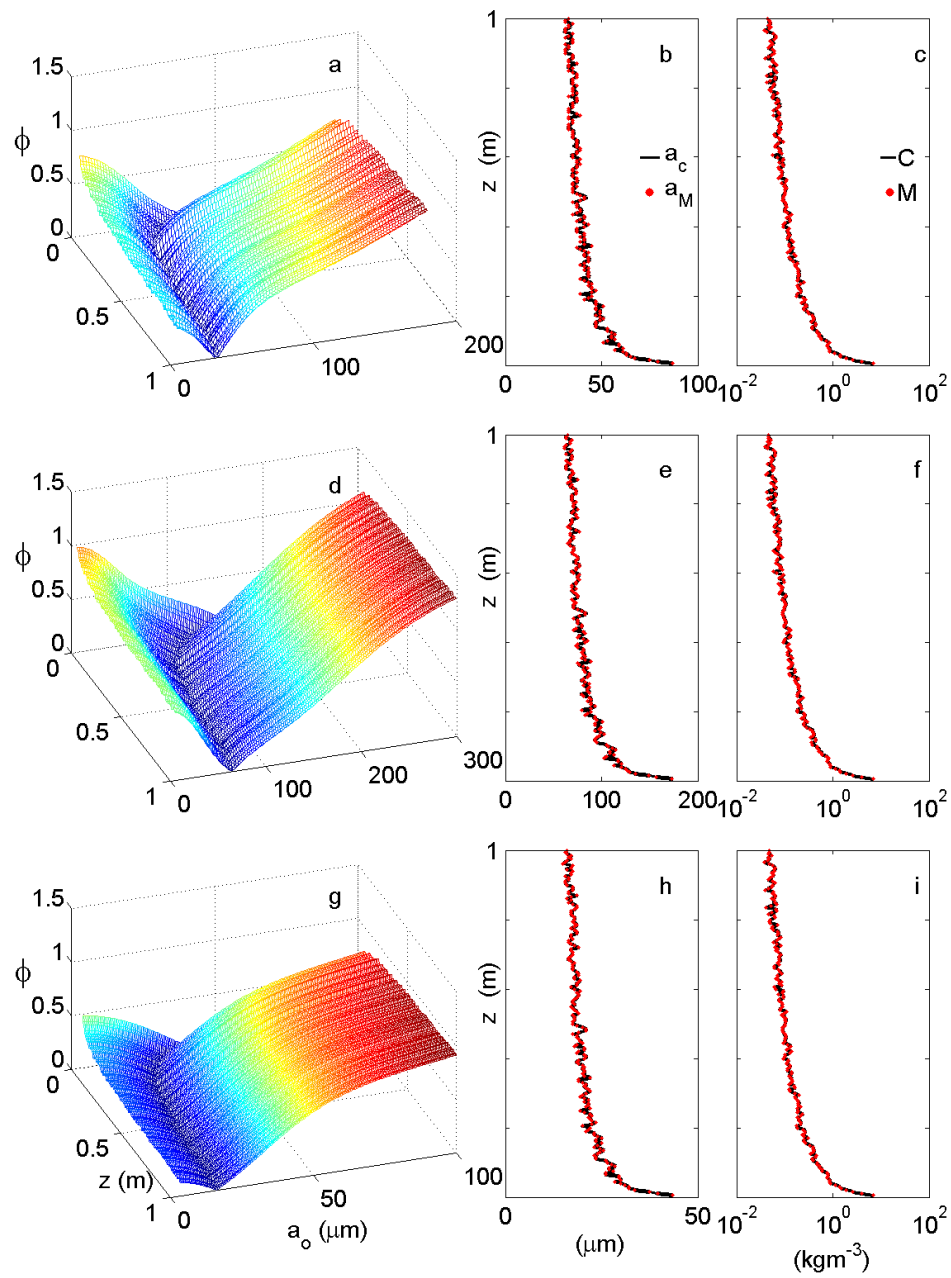takes o/p from % n:\mat5work\sizescatter\abs_inversion\inv_press_c_a3b.m

1484

1485
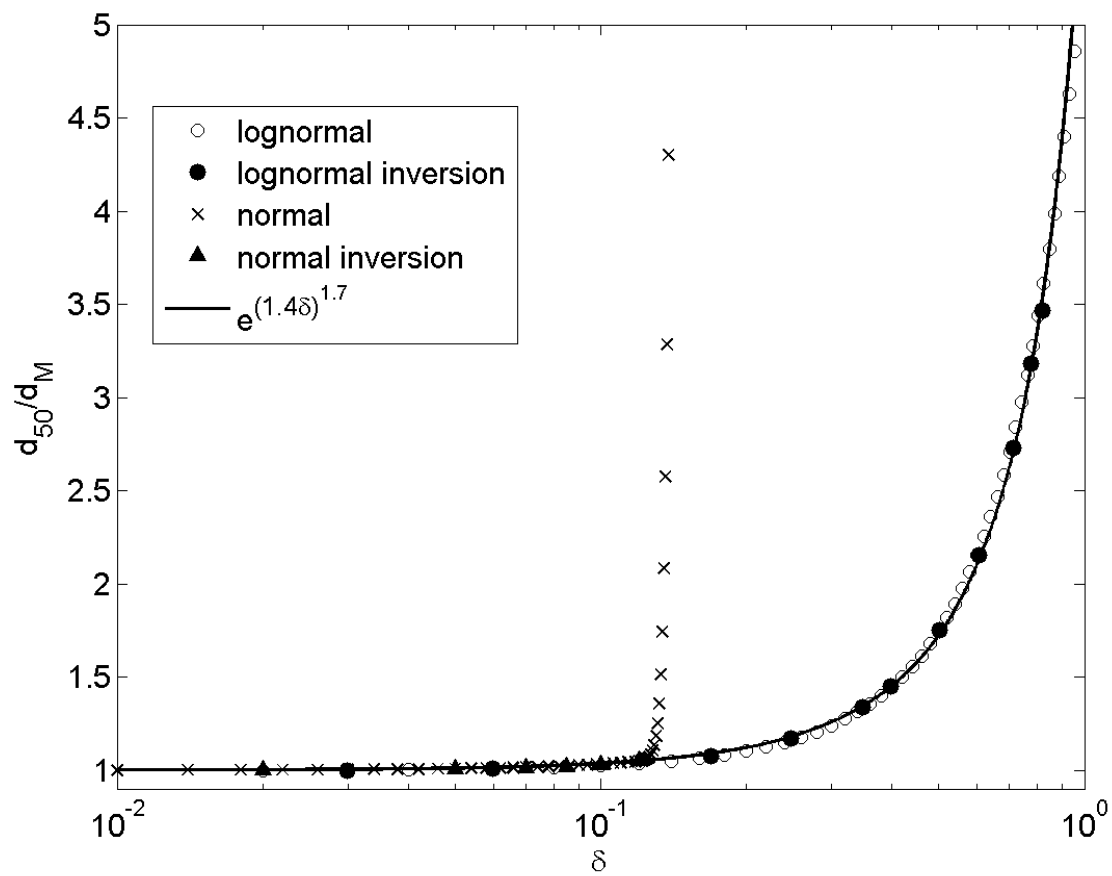
1486

1487

Fig 13 n:\mat5work\sizescatter\abs_inversion\inv_c_a4.m   26-10-12
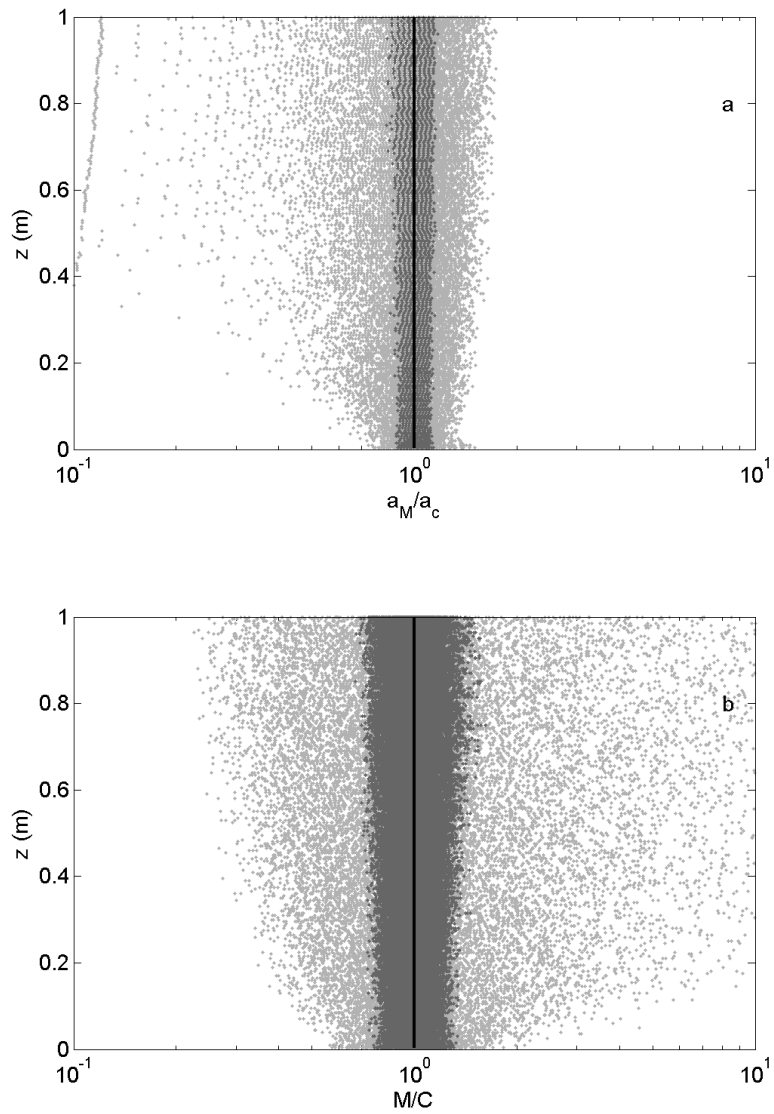n:\mat5work\sizescatter\ben-mineral\msize_nsize2.m 26/10/12

1490

1491

1492

1493

Fig A2.1. n:\mat5work\sizescatter\abs_inversion\size_inv1b.m 19/11/12
run n:\mat5work\sizescatter\abs_inversion\press1.m
run n:\mat5work\sizescatter\abs_inversion\inv_press_c_a2.m

1494
1495
1496
1497
1498

1499

1500

1501
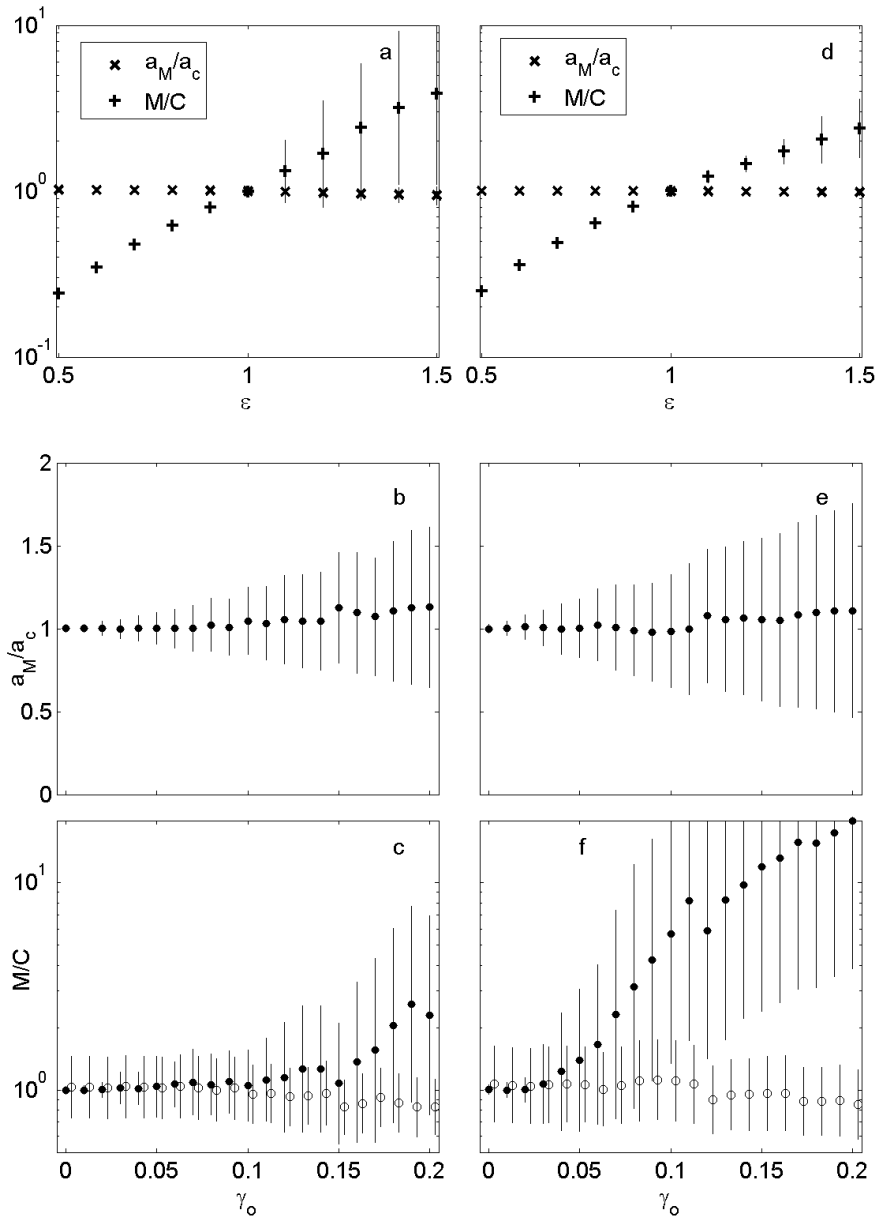

1502

1503

Fig A3.1. n:\mat5work\sizescatter\abs_inversion\plot_inv_c_a_comp.m   6-8-12
plots o/p from % n:\mat5work\sizescatter\abs_inversion\inv_c_a2b.m   6-8-12
compare pair o/p with combined 3 freq o/p

1507

1508
1509
1510 $a = 1.5a_c$ $a = a_c/1.5$
1511   Fig A4.1 n:\mat5work\sizescatter\abs_inversion\plot_err_stats3b.m
1512   takes o/p from % n:\mat5work\sizescatter\abs_inversion\inv_c_a2c_b.m
1513   takes o/p from % n:\mat5work\sizescatter\abs_inversion\inv_c_a2c_2b.m
1514   takes o/p from % n:\mat5work\sizescatter\abs_inversion\inv_c_2c_2b.m